Weak Grid Characteristic Analysis and Operating Mode Selection for Voltage Support Enhancement of Wind Farms Connected to MMC-HVDC During Asymmetric Faults

Jianan Yan, *Student Member, IEEE*, Xiaojie Shi, *Senior Member, IEEE*, Tao Liu, *Student Member, IEEE*, Zhiqiang Wang, *Senior Member, IEEE*, Li Zhang, *Senior Member, IEEE*, and Lei Lin, *Senior Member, IEEE*

***Abstract*—The voltage support functions have been mandated in grid codes to help wind turbines (WTs) ride through ac faults. In a modular multilevel converter-based high voltage dc (MMC-HVDC) system for wind farm integration, particularly in scenarios where there is no conventional synchronous generator at the sending end, the MMC adopts voltage-frequency control to form an ac grid. Such grid, however, is found to have a distinctive weak characteristic, which significantly alters the relationship between the point of common coupling voltage and the current injected by WTs and makes existing voltage support modeling methods and control strategies for grid-connected inverters inapplicable to the WTs connected to MMC-HVDC. To enhance the voltage support performance for the WTs, this article aims to elaborate on the weak grid characteristic of the voltage formed by the MMC. To streamline the analysis, the concept of generalized fault impedance is first proposed to eliminate the need for numerous models built for scenarios with different network structures, negative sequence controls, fault types, and transformer winding configurations. Additionally, this article categorizes the operating modes of the MMC and utilizes the piecewise modeling method to derive precise control equations in each operating mode, based on which the weak grid characteristic is thoroughly discussed. Subsequently, to avoid globally identifying the optimal voltage support point, an operating mode selection method prior to the voltage support realization is proposed. Finally, the above modeling method and analysis are verified through control-hardware-in-the-loop experiments.**

***Index Terms*—Generalized fault impedance, piecewise modeling method, target operating mode, voltage support, voltage-frequency control, weak grid characteristic.**

Received 3 January 2025; revised 9 May 2025 and 30 August 2025; accepted 20 September 2025. Date of publication 23 September 2025; date of current version 13 November 2025. This work was supported in part by the National Natural Science Foundation of China under Grant U23A20656 and in part by the Smart Grid-National Science and Technology Major Project under Grant 2024ZD0802600. Recommended for publication by Associate Editor X. Zhang. *(Corresponding author: Xiaojie Shi.)*

The authors are with the State Key Laboratory of Advanced Electromagnetic Technology, School of Electrical and Electronic Engineering, Huazhong University of Science and Technology, Wuhan 430074, China (e-mail: j_yan@hust.edu.cn; xiaojie_shi@hust.edu.cn; tao_liu@hust.edu.cn; zhiqiangwang@hust.edu.cn; zhangli_frank@hust.edu.cn; linlei@hust.edu.cn).

Color versions of one or more figures in this article are available at https://doi.org/10.1109/TPEL.2025.3613420.

Digital Object Identifier 10.1109/TPEL.2025.3613420

NOMENCLATURE

$\boldsymbol{e}_{\mathrm{MMC}}$, $\boldsymbol{e}_{\mathrm{WT}}$	Terminal voltages of the modular multilevel converter (MMC) and wind turbine (WT).
$\boldsymbol{i}_{\mathrm{MMC}}$, $\boldsymbol{i}_{\mathrm{WT}}$	Currents of the MMC and WT.
$\boldsymbol{v}_{\mathrm{MMC}}$, $\boldsymbol{v}_{\mathrm{WT}}$	Voltages at the point of connection of the MMC (PoC-MMC) and the point of common coupling (PCC) of the WT.
$\boldsymbol{v}_{\mathrm{F}}$, $\boldsymbol{i}_{\mathrm{F}}$	Fault voltage and current.
$\boldsymbol{z}^{-}_{\mathrm{eMMC}}$, $\boldsymbol{z}^{-}_{\mathrm{eWT}}$	Negative sequence equivalent impedances of the MMC and WT.
$\boldsymbol{Z}_{\mathrm{L}}$	Total impedance of the transmission line.
$\boldsymbol{Z}_{\mathrm{LMMC}}$, $\boldsymbol{Z}_{\mathrm{LWT}}$	Transmission line impedances on the MMC and WT sides.
X_{T1}, X_{T2}	Transformer reactance.
α	Fault location ($\alpha = \boldsymbol{Z}_{\mathrm{LMMC}}/\boldsymbol{Z}_{\mathrm{L}}$).
X_{cMMC}, X_{cWT}	Output reactance of the MMC and WT.
$\boldsymbol{Z}_{\mathrm{MMC}}$, $\boldsymbol{Z}_{\mathrm{WT}}$	Equivalent impedances on the MMC and WT sides ($\boldsymbol{Z}_{\mathrm{MMC}} = \boldsymbol{Z}_{\mathrm{cMMC}} + jX_{\mathrm{T1}} + \alpha\boldsymbol{Z}_{\mathrm{L}} = R_{\mathrm{MMC}} + jX_{\mathrm{MMC}}$).
$\boldsymbol{Z}_{\mathrm{g}}$	Fault/grounding impedance.
$\boldsymbol{z}_{\mathrm{F}}$	Generalized fault impedance ($\boldsymbol{z}_{\mathrm{F}} = r_{\mathrm{F}} + jx_{\mathrm{F}}$).
θ_{MMC}, θ_{WT}	Phase angle for Park transformation in the MMC and WT.
$\theta_{\boldsymbol{X}}$, $\lvert\boldsymbol{X}\rvert$	Direction angle and amplitude of vector $\boldsymbol{X}$.
Variables in lowercase and uppercase	Instantaneous values and steady-state values of variables.
Superscript: +, −, 0, and ∗	Positive, negative, and zero sequence components and reference of variables.
Superscript: a, b, and c	Phase a, b, and c components of three-phase variables.
Superscript: (m)	Fault types. (1): single-line-to-ground (SLG); (2): line-to-line (LL); (11): line-to-line-to-ground (LLG).
Subscript: d, q	*d*- and *q*-axes components of variables.

I. Introduction

With advantages such as high cost-effectiveness, efficiency, control flexibility and stability, and the ability of asynchronous interconnection [1], the flexible high voltage dc (HVDC) scheme is preferred for long-distance transmission of both onshore and offshore wind power, such as the Zhangbei flexible dc project [2] and the Rudong offshore wind power project [3] in China. In such system, wind farms and an MMC-based sending-end station connect to an ac network that can be isolated from the main power grid by a dc transmission line, as illustrated in Fig. 1. Fault ride-through (FRT) capability becomes mandatory in grid codes of many countries to avoid tripping of large-scale WTs [4], [5], [6]. Maintaining the PCC voltage of WTs within the endurable range is one of the FRT requirements, demanding controls for positive and negative sequence voltages during asymmetric faults.

For grid-connected inverters, the equivalent infinite voltage source of both strong and weak power grids provides a stiff positive sequence voltage, regardless of variations in the amplitudes and angles of the injected currents [7], [8], [9], [10]. It is widely recognized that the voltage at the fault point can be approximated based on the fault/grounding impedance and Thevenin's impedance before the infinite voltage source [11], and the voltage deviation on the inverter-side transmission lines from the fault point to the PCC can be utilized to support the PCC voltages of the inverters. Consequently, the voltage at the fault point is normally treated as the dropped grid voltage to establish the model for voltage support analysis in grid-connected systems [12], [13], [14], [15], [16], [17], [18], [19]. Based on such assumption, substantial research efforts have been taken to investigate voltage support strategies. The basic principle involves injecting positive sequence currents to enhance the positive sequence voltage and negative sequence currents to alleviate the voltage imbalance. Associated optimal control methods have been proposed to satisfy diverse needs by leveraging the current capacity of the inverters, including positive and negative sequence voltage objectives [12], [13], [14], [15], types of line impedances [16], [17], and communication conditions among multi-inverters [18], [19].

Different from the grid-connected systems assumed in all references above, since no conventional power resources such as synchronous generators exist in the sending-end system, the MMC should implement grid-forming control to establish an ac grid. Given its capability to maintain the PoC-MMC voltage and frequency at their nominal values during normal operation, voltage-frequency (VF) control is typically employed [20], [21], [22], [23], [24], [25], [26]. However, physically limited by the low current capacity and dc voltage of the MMC, the positive sequence terminal voltage generated by the VF control during ac faults can be time-varying and relatively weak. Such characteristic significantly changes the relationship between the PCC voltage and the currents injected from WTs. As illustrated in Fig. 2, when injecting the positive ($i^{+}_{qWT} < 0$) and negative sequence ($i^{-}_{qWT} < 0$, decoupled by a negative sequence phase-locked loop (PLL) [27]) inductive reactive current at 2.5 s, the positive sequence voltage of the WT decreases, instead of increasing,

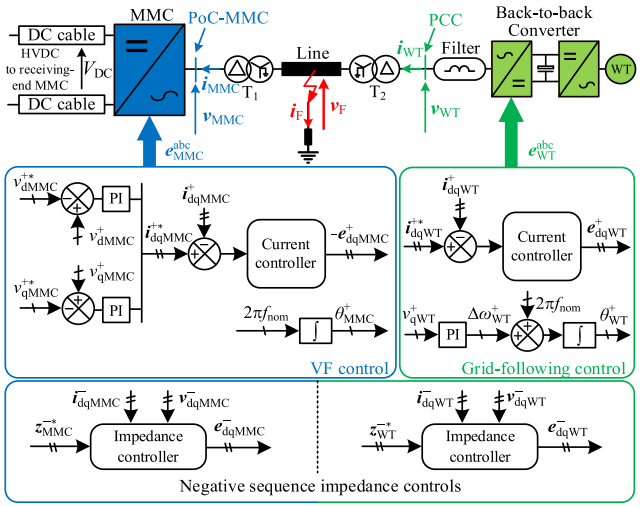

Fig. 1. Sending-end MMC-WTs system with positive and negative sequence controls.

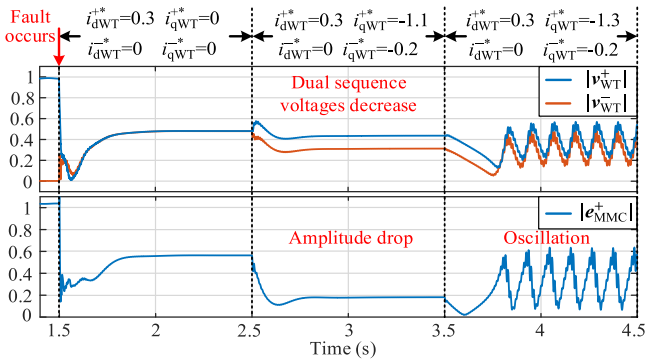

Fig. 2. Simulation waveforms demonstrating the weak grid characteristic. [Parameters: CL-VSR, I^{+}_{limMMC}= 0.9 p.u., v^{+*}_{dMMC}= 0.5 p.u., i^{-*}_{dqMMC}= 0. Fault: LLG, $\alpha = 0\%$, $\boldsymbol{Z}_g$= 0.1323 p.u. Units: per unit (p.u.)].

thus incapable of voltage support. Furthermore, when an additional positive sequence inductive reactive current is further generated at 3.5 s, a terminal voltage oscillation occurs. The amplitude drop and oscillation of the positive sequence terminal voltage during voltage support both indicate a distinctive weak grid characteristic. This weak grid characteristic degrades the grid-forming capability of the MMC and simultaneously causes the positive sequence PCC voltage of WTs to drop and oscillate.

The conventional weak power grid is defined as an infinite voltage source with high Thevenin's impedance [28], [29], [30], [31], [32]. While both the conventional weak power grid and the ac grid formed by the MMC can exacerbate the voltage sags at the fault point, the underlying causes differ: in the former scenario, the high Thevenin impedance is the primary factor, whereas in the latter case, the current capacity and dc voltage constraints of the MMC play a significant role. Therefore, these physical constraints must be considered when designing voltage support enhancement control methods, which can make the modeling methods, voltage support theories, and control strategies for grid-connected inverters inapplicable.

To satisfy these physical constraints, the current and modulation voltage limiting functions must be configured in the VF control. A current limiter (CL) is typically incorporated to limit the fault current from the MMC [20], [21], [22], [23], [24], [25], [26]. Moreover, two categories of voltage limiting methods are commonly used in the existing literature [22], [23], [24], [25], [26]: the voltage set-point reduction (VSR) method [22], [26], and the modulation voltage limiter (MVL) [23], [24], [25], [26]. These two limiting structures, i.e., CL-VSR and CL-MVL, can be integrated into the VF control. To prevent overcurrent and overmodulation, the limiters should be deliberately designed when integrating the negative sequence controls. Besides, negative sequence coordination between the MMC and WTs has also been investigated to facilitate current limiting [22], [23], [24]. Shi et al. [22] suggested that both the MMC and WTs eliminate their negative sequence currents. Additionally, for a fast postfault recovery, an extra negative sequence voltage outer loop with a CL is proposed in this article. Given that WTs have a higher current capacity than the MMC, Li et al. [23] and Yan et al. [24] eliminated the negative sequence current of the MMC and enable an even distribution of the negative sequence currents among WTs through a virtual impedance control.

Aiming at the current limiting objective alone, the methods mentioned above employ adaptive model-free controllers such as proportional-integral (PI) controllers and limiters, which are straightforward, particularly in a converter-dominated ac grid. However, these methods overlook the voltage variations resulting from the weak grid characteristic and cannot achieve maximum voltage support. Therefore, it is necessary to elaborate on the weak grid characteristic under the maximum voltage support objective. In this context, the current limiting objective becomes a constraint condition.

Sequence circuits are commonly used to analyze asymmetric fault characteristics of the sending-end system. In the sequence circuit, various equivalent models for the MMC and WT have been developed to align with the negative sequence controls mentioned above. Shi et al. [22] uniformly adopted a voltage source representation for the negative sequence voltage closed-loop control in the MMC and zero-current control in the WT. However, this method necessitates the establishment of various mathematical relationships under different fault types. Involving numerous variables, these relationships typically have high dimensions and pose great challenges in analyzing the weak grid characteristic. Furthermore, Li et al. [23] and Yan et al. [24] suggested using current sources to represent the negative sequence current control in the MMC, while employing a constant impedance to model the negative sequence voltage-current droop control or without control in the WT. This method presents similar challenges. Additionally, the variety of negative sequence equivalent models increases the complexity of the weak grid characteristic analysis. Therefore, a unified and more effective analytical sequence circuit is required.

The strong nonlinearity of the CL and MVL makes the modeling of the VF control challenging. The piecewise method is an effective tool for studying nonlinear control systems with distinct inflection points. This method divides the entire control system into multiple intervals, allowing the characteristics within each interval to be represented by simpler mathematical models. For example, Huang et al. [33], Rokrok et al. [34], Wang et al. [35], and Sun et al. [36] employed this method to assess the transient stability of grid-forming converters separately under the current saturation and current unsaturation modes. Therefore, the piecewise modeling method will be adopted in this article to address the strong nonlinearity of the limiters, facilitating the development of precise control equations.

This article aims to establish a mathematical model of the sending-end MMC-WTs system, analyze the weak grid characteristic, and then propose a target operating mode selection method. The key contributions are summarized as follows.

1) Defines the generalized fault impedance (GFI) as an independent variable. Enabling a unified equivalent circuit, the GFI eliminates structural differences in negative/zero sequence circuits caused by various ac networks, negative sequence controls, fault types, and transformer winding configurations, while maintaining the differential information. Additionally, by establishing the mapping between the GFI and positive sequence terminal voltage, the influence of the fault branch on the weak grid characteristic can be captured without the need to consider each variable within the fault branch. The proposed unified equivalent circuit significantly simplifies the weak grid characteristic analysis by reducing the complexity and dimension and is also applicable to symmetric faults.
2) Defines the operating modes of the sending-end MMC with two limiting structures, i.e., CL-VSR and CL-MVL, and derives precise control equations to mathematically model the VF control in each operating mode.
3) Characterizes the positive sequence terminal voltage in different operating modes and identifies their transition process through the numerical traversal of the independent variables, intuitively revealing distinctions between the power grid and ac grid formed by the MMC.
4) Provides guidance on the optimal operating mode selection under different types of asymmetric faults, which avoids globally identifying the optimal operating point and reduces the computational burden on the controllers.

The rest of this article is organized as follows. In Section II, a unified equivalent circuit of the sending-end system is derived after defining the GFI. Subsequently, the operating modes of the MMC are defined, and a precise mathematical model of the sending-end system is established in Section III. On this basis, the weak grid characteristic is analyzed through a numerical traversal in Section IV. Section V proposes a method for optimally selecting the target operating modes under different types of faults. Section VI presents the control-hardware-in-the-loop (CHIL) experimental results based on Typhoon 604 to verify the proposed mathematical model and the weak grid characteristic. Finally, Section VII concludes this article.

II. Equivalent Circuits for Weak Grid Characteristic Analysis

In this article, the type-4 WT with a grid-following inverter is discussed as an example. Moreover, Dy_g and Y_gd windings are

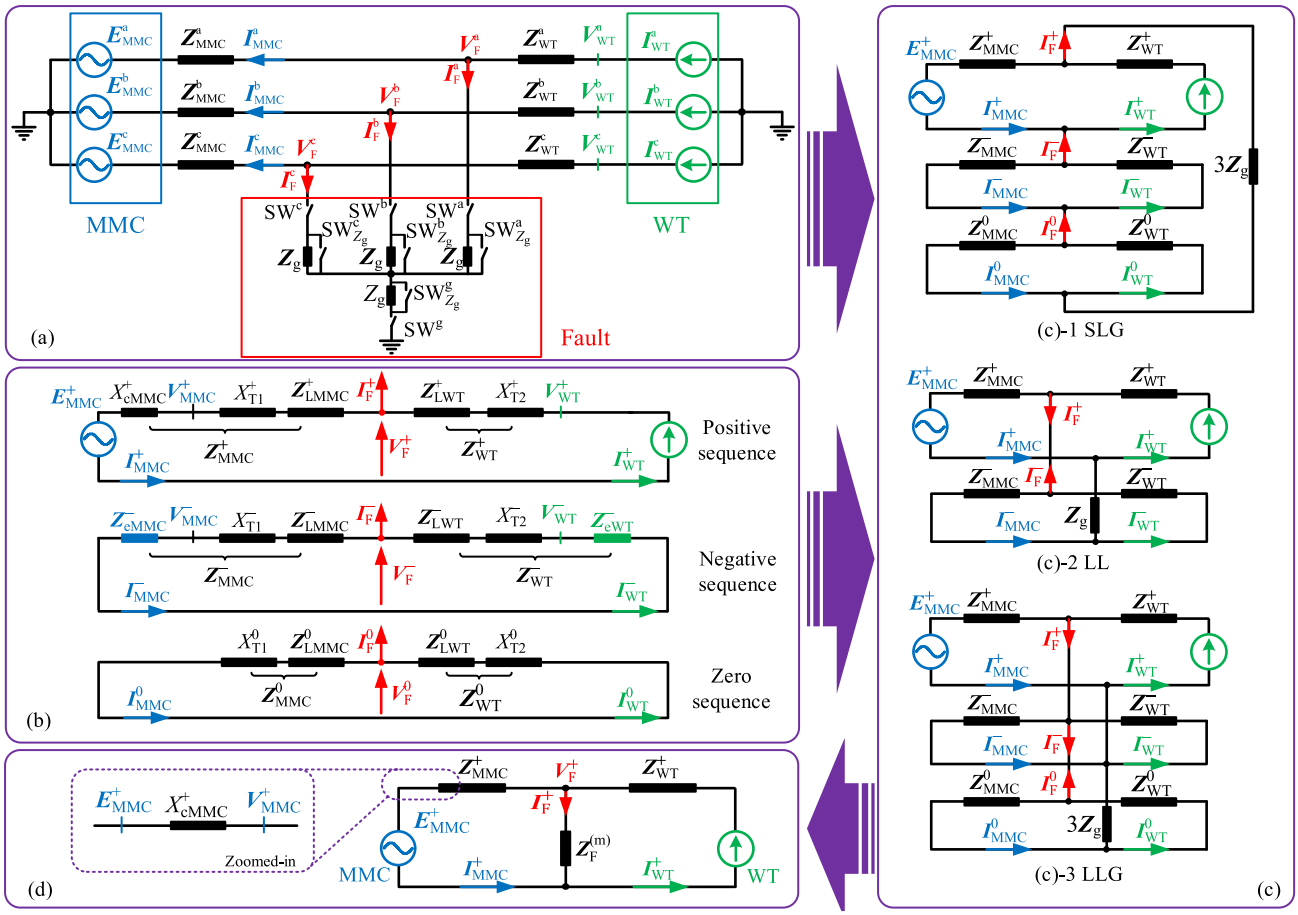

Fig. 3. Equivalent circuits of the sending-end system. (a) Simplified three-phase circuit during faults. (b) Positive, negative and zero sequence circuits. (c) Sequence circuits of three types of asymmetric faults. (d) Unified equivalent circuit under different types of faults.

TABLE I
IMPEDANCE CHARACTERISTICS OF TYPICAL NEGATIVE SEQUENCE CONTROLS

Typical negative sequence controls	Equivalent circuit models in the literature	Impedance characteristics
Zero-current control/ current control	Current source [23]–[24] / voltage source [22]	Infinite impedance
Voltage closed-loop control with a CL	Voltage source [22]	Dynamic impedance
Voltage-current droop control	Constant impedance (designed by the droop coefficient) [24], [27]	Adjustable impedance
Without control	Impedance of the filter [23]-[24]	Constant impedance

used in transformers T_1 and T_2, respectively, to prevent zero sequence currents from traversing both the MMC and WTs, while providing effective grounding for the sending-end MMC-WTs system. The simplified three-phase circuit with common types of faults is shown in Fig. 3(a). The WTs in wind farms are aggregated into one equivalent WT to emphasize ensemble output characteristics for the following analysis [37], [38].

The equivalent circuit models for typical negative sequence controls are summarized in Table I. These various equivalent circuits make it challenging to analyze the impact of control parameters on the positive sequence terminal voltage of the MMC and to capture the weak grid characteristic. To address this issue, the circuit models of the typical negative sequence controls are standardized as impedances in this article, as shown in Fig. 3(b), and their corresponding characteristics are given in the subsequent column in Table I. The negative sequence equivalent impedances are expressed as

$$\boldsymbol{Z}^{-}_{\mathrm{eMMC}} = \overline{\left(\frac{\boldsymbol{V}^{-}_{\mathrm{MMC}}}{\boldsymbol{I}^{-}_{\mathrm{MMC}}}\right)}, \boldsymbol{Z}^{-}_{\mathrm{eWT}} = \overline{\left(\frac{\boldsymbol{V}^{-}_{\mathrm{WT}}}{-\boldsymbol{I}^{-}_{\mathrm{WT}}}\right)} \tag{1}$$

where $\bar{\boldsymbol{X}}$ denotes the conjugate of $\boldsymbol{X}$. The negative sequence impedance controller, as presented in Fig. 1, utilizes the admittance-current control (ACC), whose detailed control process can refer to [27].

Due to the wye windings of the transformers on the ac line side, the zero sequence circuit exhibits passive impedance characteristics. Even with alternative winding configurations, such as $Y_g y_g$, active zero sequence circuits can also be represented as equivalent impedances with zero sequence impedance control, similar to the negative sequence control.

The equivalent sequence circuits for three types of asymmetric faults are illustrated in Fig. 3(c), with the detailed derivation provided in [22]. Utilizing the equivalent impedance of the

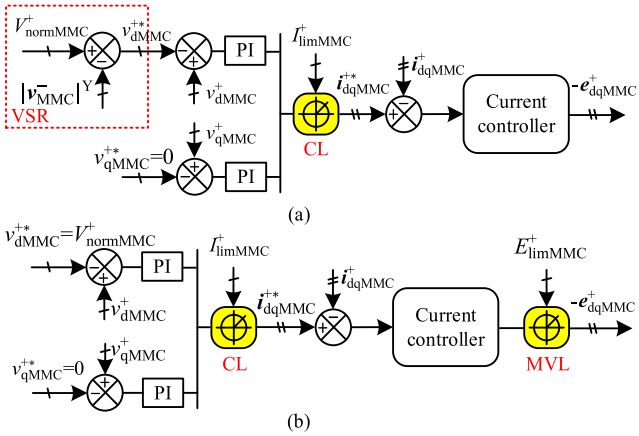

Fig. 4. Limiting structures of the VF control. (a) CL-VSR. (b) CL-MVL.

negative and zero sequence controls, the GFI can be defined as a combination of the negative and zero sequence circuits and the fault/grounding impedance, as depicted in Fig. 3(d). The GFI can be any value in the four quadrants and expressed as

$$\begin{cases} \boldsymbol{Z}_{\mathrm{F}}^{(1)} = \boldsymbol{Z}_{\mathrm{MMC}}^{-} // \boldsymbol{Z}_{\mathrm{WT}}^{-} + \boldsymbol{Z}_{\mathrm{MMC}}^{0} // \boldsymbol{Z}_{\mathrm{WT}}^{0} + 3\boldsymbol{Z}_{\mathrm{g}} \\ \boldsymbol{Z}_{\mathrm{F}}^{(2)} = \boldsymbol{Z}_{\mathrm{MMC}}^{-} // \boldsymbol{Z}_{\mathrm{WT}}^{-} + \boldsymbol{Z}_{\mathrm{g}} \\ \boldsymbol{Z}_{\mathrm{F}}^{(1,1)} = (\boldsymbol{Z}_{\mathrm{MMC}}^{-} // \boldsymbol{Z}_{\mathrm{WT}}^{-}) // (\boldsymbol{Z}_{\mathrm{MMC}}^{0} // \boldsymbol{Z}_{\mathrm{WT}}^{0} + 3\boldsymbol{Z}_{\mathrm{g}}) \end{cases} \tag{2}$$

where // represents the parallel operator.

Three state variables are selected to describe the weak grid characteristic, i.e., $\boldsymbol{E}_{\mathrm{MMC}}^{+}$, $\boldsymbol{I}_{\mathrm{MMC}}^{+}$, and $\boldsymbol{V}_{\mathrm{MMC}}^{+}$. According to Fig. 3(d), the state variables can be determined by three independent variables: $\boldsymbol{I}_{\mathrm{WT}}^{+}$, representing the positive sequence current of the WT; α, representing the fault location; $\boldsymbol{Z}_{\mathrm{F}}^{(\mathrm{m})}$, representing the combined effect of fault type, fault/grounding impedance, negative sequence controls, and zero sequence circuits.

III. Mathematical Modeling of the Sending-End System

To analyze the influence of the independent variables on the state variables, a mathematical model of the sending-end system is established, incorporating the network equations, connection equations, and control equations. Here, the connection equations serve as a bridge between the network equations and control equations. The control equations with the two limiting structures of the VF control, as illustrated in Fig. 4, will be thoroughly discussed. Moreover, static stability criteria are also proposed to screen the effective steady-state operating points.

A. Network Equations and Connection Equations

According to the unified equivalent circuit presented in Fig. 3(d), utilizing KCL and KVL, the network equation and connection equation are, respectively, derived as

$$\boldsymbol{E}_{\mathrm{MMC}}^{+} = (\boldsymbol{I}_{\mathrm{WT}}^{+} - \boldsymbol{I}_{\mathrm{MMC}}^{+})\boldsymbol{Z}_{\mathrm{F}}^{(\mathrm{m})} - \boldsymbol{I}_{\mathrm{MMC}}^{+}\boldsymbol{Z}_{\mathrm{MMC}}^{+} \tag{3}$$

$$\boldsymbol{E}_{\mathrm{MMC}}^{+} = \boldsymbol{V}_{\mathrm{MMC}}^{+} - j\boldsymbol{I}_{\mathrm{MMC}}^{+}X_{\mathrm{cMMC}}^{+}. \tag{4}$$

Since dq-axes components, instead of vectors, are employed in the controllers, it is essential to transition the network and connection equations into the dq coordinates to align with the control equations. The phase angle of the MMC dq-frame is generated by the integral of rated frequency f_{nom}, while that of the WT dq-frame is established by a positive sequence PLL, whose dynamic process can be mathematically expressed as

$$\Delta\omega_{\mathrm{WT}}^{+} = k_{\mathrm{p\_PLL}}^{+} v_{\mathrm{qWT}}^{+} + k_{\mathrm{i\_PLL}}^{+} \int v_{\mathrm{qWT}}^{+} dt \tag{5}$$

$$\theta_{\mathrm{WT}}^{+} = \int (2\pi \cdot f_{\mathrm{WT}})dt = \int (2\pi \cdot f_{\mathrm{nom}} + \Delta\omega_{\mathrm{WT}}^{+})dt. \tag{6}$$

Under these two frames, the voltages and currents of the MMC and the WT can be obtained as

$$\boldsymbol{E}_{\mathrm{MMC}}^{+} = \begin{bmatrix} E_{\mathrm{dMMC}}^{+} \\ E_{\mathrm{qMMC}}^{+} \end{bmatrix}_{\theta_{\mathrm{MMC}}^{+}} \text{or} = \begin{bmatrix} \widehat{E}_{\mathrm{dMMC}}^{+} \\ \widehat{E}_{\mathrm{qMMC}}^{+} \end{bmatrix}_{\theta_{\mathrm{WT}}^{+}} \tag{7}$$

$$\boldsymbol{V}_{\mathrm{MMC}}^{+} = \begin{bmatrix} V_{\mathrm{dMMC}}^{+} \\ V_{\mathrm{qMMC}}^{+} \end{bmatrix}_{\theta_{\mathrm{MMC}}^{+}} \text{or} = \begin{bmatrix} \widehat{V}_{\mathrm{dMMC}}^{+} \\ \widehat{V}_{\mathrm{qMMC}}^{+} \end{bmatrix}_{\theta_{\mathrm{WT}}^{+}} \tag{8}$$

$$\boldsymbol{I}_{\mathrm{MMC}}^{+} = \begin{bmatrix} I_{\mathrm{dMMC}}^{+} \\ I_{\mathrm{qMMC}}^{+} \end{bmatrix}_{\theta_{\mathrm{MMC}}^{+}} \text{or} = \begin{bmatrix} \widehat{I}_{\mathrm{dMMC}}^{+} \\ \widehat{I}_{\mathrm{qMMC}}^{+} \end{bmatrix}_{\theta_{\mathrm{WT}}^{+}} \tag{9}$$

$$\boldsymbol{I}_{\mathrm{WT}}^{+} = \begin{bmatrix} \left|\boldsymbol{I}_{\mathrm{WT}}^{+}\right| \cos(\varphi_{\mathrm{WT}}^{+}) \\ \boldsymbol{I}_{\mathrm{WT}}^{+} \sin(\varphi_{\mathrm{WT}}^{+}) \end{bmatrix} = \begin{bmatrix} I_{\mathrm{dWT}}^{+} \\ I_{\mathrm{qWT}}^{+} \end{bmatrix}_{\theta_{\mathrm{WT}}^{+}} \text{or} = \begin{bmatrix} \widehat{I}_{\mathrm{dWT}}^{+} \\ \widehat{I}_{\mathrm{qWT}}^{+} \end{bmatrix}_{\theta_{\mathrm{MMC}}^{+}}. \tag{10}$$

In the WT frame, $\boldsymbol{V}_{\mathrm{WT}}^{+}$ is locked to the d-axis by the PLL, i.e., I_{dWT}^{+} aligns with the voltage vector and represents the active power component, while I_{qWT}^{+} is orthogonal to the voltage vector and determines the reactive power. For ease of description, map the dq-axes currents of the WT into the MMC frame, with the transformation matrix $\boldsymbol{T}_{\mathrm{WT\text{-}MMC}}$ expressed as

$$\boldsymbol{T}_{\mathrm{WT-MMC}} = \begin{bmatrix} \cos(\theta_{\mathrm{MMC}}^{+} - \theta_{\mathrm{WT}}^{+}) & \sin(\theta_{\mathrm{MMC}}^{+} - \theta_{\mathrm{WT}}^{+}) \\ -\sin(\theta_{\mathrm{MMC}}^{+} - \theta_{\mathrm{WT}}^{+}) & \cos(\theta_{\mathrm{MMC}}^{+} - \theta_{\mathrm{WT}}^{+}) \end{bmatrix}. \tag{11}$$

Thus, the dq-axes currents of the WT in the MMC frame can be obtained as

$$\begin{bmatrix} \widehat{I}_{\mathrm{dWT}}^{+} \\ \widehat{I}_{\mathrm{qWT}}^{+} \end{bmatrix} = \boldsymbol{T}_{\mathrm{WT-MMC}} \begin{bmatrix} I_{\mathrm{dWT}}^{+} \\ I_{\mathrm{qWT}}^{+} \end{bmatrix}. \tag{12}$$

The vector diagram under the two frames is illustrated in Fig. 5, where the dq-axes and vectors of the MMC and WT are in blue and green, respectively, and fault vectors are in red. It is observed that the phase angle discrepancy of these two frames equals the sum of the phase angle of the MMC voltage vector ($\theta_{\boldsymbol{V}_{\mathrm{MMC}}^{+}}$) and power angle δ^{+} caused by the power flow variations, leading to

$$\theta_{\mathrm{WT}}^{+} - \theta_{\mathrm{MMC}}^{+} = \theta_{\boldsymbol{V}_{\mathrm{MMC}}^{+}} + \delta^{+}. \tag{13}$$

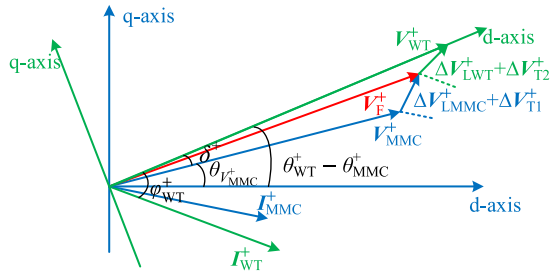

Fig. 5. Vector diagram under the two frames.

Therefore, the transformation matrix can be specified as

$$\boldsymbol{T}_{\mathrm{WT-MMC}} = \begin{bmatrix} \frac{V^+_{\mathrm{dMMC}}}{\sqrt{V^{+\ 2}_{\mathrm{dMMC}}+V^{+\ 2}_{\mathrm{qMMC}}}} & -\frac{V^+_{\mathrm{qMMC}}}{\sqrt{V^{+\ 2}_{\mathrm{dMMC}}+V^{+\ 2}_{\mathrm{qMMC}}}} \\ \frac{V^+_{\mathrm{qMMC}}}{\sqrt{V^{+\ 2}_{\mathrm{dMMC}}+V^{+\ 2}_{\mathrm{qMMC}}}} & \frac{V^+_{\mathrm{dMMC}}}{\sqrt{V^{+\ 2}_{\mathrm{dMMC}}+V^{+\ 2}_{\mathrm{qMMC}}}} \end{bmatrix} \times \begin{bmatrix} \cos\delta^+ & -\sin\delta^+ \\ \sin\delta^+ & \cos\delta^+ \end{bmatrix}. \tag{14}$$

Substituting (7)–(12) into (3) and (4), the dq-axes forms of the network and connection equations can be obtained as

$$\begin{bmatrix} E^+_{\mathrm{dMMC}} \\ E^+_{\mathrm{qMMC}} \end{bmatrix} = \begin{bmatrix} R^{(\mathrm{m})}_{\mathrm{F}} & -X^{(\mathrm{m})}_{\mathrm{F}} \\ X^{(\mathrm{m})}_{\mathrm{F}} & R^{(\mathrm{m})}_{\mathrm{F}} \end{bmatrix} \left(\boldsymbol{T}_{\mathrm{WT-MMC}} \begin{bmatrix} I^+_{\mathrm{dWT}} \\ I^+_{\mathrm{qWT}} \end{bmatrix} - \begin{bmatrix} I^+_{\mathrm{dMMC}} \\ I^+_{\mathrm{qMMC}} \end{bmatrix} \right) - \begin{bmatrix} R^+_{\mathrm{MMC}} & -X^+_{\mathrm{MMC}} \\ X^+_{\mathrm{MMC}} & R^+_{\mathrm{MMC}} \end{bmatrix} \begin{bmatrix} I^+_{\mathrm{dMMC}} \\ I^+_{\mathrm{qMMC}} \end{bmatrix} \tag{15}$$

$$\begin{bmatrix} E^+_{\mathrm{dMMC}} \\ E^+_{\mathrm{qMMC}} \end{bmatrix} = \begin{bmatrix} V^+_{\mathrm{dMMC}} \\ V^+_{\mathrm{qMMC}} \end{bmatrix} - X^+_{\mathrm{cMMC}} \begin{bmatrix} -I^+_{\mathrm{qMMC}} \\ I^+_{\mathrm{dMMC}} \end{bmatrix}. \tag{16}$$

B. Control Equations With the CL-VSR Limiting Structure

With the CL-VSR limiting structure, the preservation of the dc voltage margin for the negative sequence control is achieved by adjusting the d-axis voltage set-point, as expressed in

$$V^{+*}_{\mathrm{dMMC}} = V^+_{\mathrm{normMMC}} - \left|\boldsymbol{V}^-_{\mathrm{MMC}}\right|^{\mathrm{Y}} \tag{17}$$

where V^+_{normMMC} is the d-axis voltage set-point during the normal operation (= 1 p.u.), and $|\boldsymbol{V}^-_{\mathrm{MMC}}|^{\mathrm{Y}}$ represents the reserved negative sequence voltage margin. This limiting structure ensures that the total modulation voltage stays within the dc voltage, thus allowing precise control of the positive sequence dq-axes currents. Similarly, to prevent an overcurrent and reserve the negative sequence current margin, a CL is incorporated into the VF control, as obtained below

$$I^+_{\mathrm{limMMC}} = I_{\mathrm{maxMMC}} - \left|\boldsymbol{I}^-_{\mathrm{MMC}}\right|^{\mathrm{Y}} \tag{18}$$

where I_{maxMMC} is the maximum allowable current, and $|\boldsymbol{I}^-_{\mathrm{MMC}}|^{\mathrm{Y}}$ represents the reserved negative sequence current margin.

The key to the control equations lies in the mathematical description of the voltage outer loop and CL. Depending on whether the CL reaches saturation, two operating modes emerge in the VF control: the voltage control mode (VCM, with an unsaturated CL) and the current limit mode (CLM, with a saturated CL). The circular limiter, as expressed in (19) [39], [40], is discussed in this article.

$$\begin{cases} X_{\mathrm{d}} = \frac{X'_{\mathrm{d}}}{\sqrt{X'^2_{\mathrm{d}}+X'^2_{\mathrm{q}}}} X_{\mathrm{lim}} \\ X_{\mathrm{q}} = \frac{X'_{\mathrm{q}}}{\sqrt{X'^2_{\mathrm{d}}+X'^2_{\mathrm{q}}}} X_{\mathrm{lim}} \end{cases} \tag{19}$$

where X, X', and X_{lim} denote the output and input variables of the limiter and its limit value, respectively.

VCM: Before hitting the CL, the VF control is in the VCM. In this mode, the PoC-MMC voltage can track its reference, and the following control equations hold:

$$\begin{cases} V^+_{\mathrm{dMMC}} = V^{+*}_{\mathrm{dMMC}} \\ V^+_{\mathrm{qMMC}} = V^{+*}_{\mathrm{qMMC}} = 0 \end{cases}. \tag{20}$$

CLM: In CLM, the CL is hit. The voltage outer loop and CL can be, respectively, described as

$$\begin{cases} I'^{+*}_{\mathrm{dMMC}} = k^+_{\mathrm{pd\_volMMC}}(V^+_{\mathrm{dMMC}} - V^{+*}_{\mathrm{dMMC}}) + k^+_{\mathrm{id\_volMMC}} \int (V^+_{\mathrm{dMMC}} - V^{+*}_{\mathrm{dMMC}})dt \\ I'^{+*}_{\mathrm{qMMC}} = k^+_{\mathrm{pq\_volMMC}}(V^+_{\mathrm{qMMC}} - V^{+*}_{\mathrm{qMMC}}) + k^+_{\mathrm{iq\_volMMC}} \int (V^+_{\mathrm{qMMC}} - V^{+*}_{\mathrm{qMMC}})dt \end{cases} \tag{21}$$

$$\begin{cases} I^{+*}_{\mathrm{dMMC}} = \frac{I'^{+*}_{\mathrm{dMMC}}}{\sqrt{I'^{+*\ 2}_{\mathrm{dMMC}}+I'^{+*\ 2}_{\mathrm{qMMC}}}} I^+_{\mathrm{limMMC}} \\ I^{+*}_{\mathrm{qMMC}} = \frac{I'^{+*}_{\mathrm{qMMC}}}{\sqrt{I'^{+*\ 2}_{\mathrm{dMMC}}+I'^{+*\ 2}_{\mathrm{qMMC}}}} I^+_{\mathrm{limMMC}} \end{cases} \tag{22}$$

where $k^+_{\mathrm{p\_volMMC}}$ and $k^+_{\mathrm{i\_volMMC}}$ are the PI coefficients of the voltage outer loop of the VF control.

Substituting (21) into (22) and letting $t \to \infty$ yield the control equations

$$\begin{cases} I^+_{\mathrm{dMMC}} = \frac{k_{\mathrm{id\_volMMC}}(V^+_{\mathrm{dMMC}} - V^{+*}_{\mathrm{dMMC}})}{\sqrt{k_{\mathrm{id\_volMMC}}{}^2(V^+_{\mathrm{dMMC}} - V^{+*}_{\mathrm{dMMC}})^2 + k_{\mathrm{iq\_volMMC}}{}^2(V^+_{\mathrm{qMMC}} - V^{+*}_{\mathrm{qMMC}})^2}} \times I^+_{\mathrm{lim\,MMC}} \\ I^+_{\mathrm{qMMC}} = \frac{k_{\mathrm{iq\_volMMC}}(V^+_{\mathrm{qMMC}} - V^{+*}_{\mathrm{qMMC}})}{\sqrt{k_{\mathrm{id\_volMMC}}{}^2(V^+_{\mathrm{dMMC}} - V^{+*}_{\mathrm{dMMC}})^2 + k_{\mathrm{iq\_volMMC}}{}^2(V^+_{\mathrm{qMMC}} - V^{+*}_{\mathrm{qMMC}})^2}} \times I^+_{\mathrm{lim\,MMC}} \end{cases}. \tag{23}$$

C. Control Equations With the CL-MVL Limiting Structure

With this limiting structure, except for the CL in (22), an MVL is employed to reserve the margin for the negative sequence modulation voltage, which satisfies

$$E^+_{\mathrm{limMMC}} = E_{\mathrm{maxMMC}} - \left|\boldsymbol{E}^-_{\mathrm{MMC}}\right|^{\mathrm{Y}} \tag{24}$$

where E_{maxMMC} is the maximum available modulation voltage, as determined by its dc voltage, and $|\boldsymbol{E}^-_{\mathrm{MMC}}|^{\mathrm{Y}}$ is the upper limit of the reserved negative sequence modulation voltage. The MVL can be described as

$$\begin{cases} E^{+*}_{\mathrm{dMMC}} = \frac{E'^{+*}_{\mathrm{dMMC}}}{\sqrt{E'^{+*2}_{\mathrm{dMMC}}+E'^{+*2}_{\mathrm{qMMC}}}} E^+_{\mathrm{limMMC}} \\ E^{+*}_{\mathrm{qMMC}} = \frac{E'^{+*}_{\mathrm{qMMC}}}{\sqrt{E'^{+*2}_{\mathrm{dMMC}}+E'^{+*2}_{\mathrm{qMMC}}}} E^+_{\mathrm{limMMC}} \end{cases}. \tag{25}$$

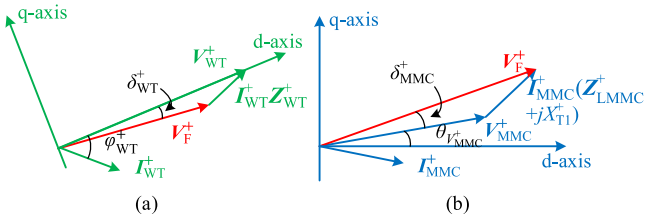

Fig. 6. Separate vector diagram for obtaining mathematical expressions of δ^+. (a) Under WT frame. (b) Under MMC frame.

Combining the status of the CL and MVL gives four modes. Among them, the case with an unsaturated CL while saturated MVL is mathematically overconstrained. After excluding such combination, the remaining three modes can be classified as the VCM, the CLM, and the modulation voltage limit mode (MVLM). Although the two limiting structures are distinct, the control equations in the VCM and CLM remain the same.

MVLM: When both the CL and MVL are saturated, the MMC operates in the MVLM, and neither the positive sequence PoC-MMC voltage nor current can accurately track their references. Under such condition, it is necessary to describe both the outer and inner loops to derive the control equations. To establish a connection between the two loops, intermediate variables I^{+*}_{dMMC} and I^{+*}_{qMMC} are introduced. Similar to the above derivation process, the control equations in the MVLM can be obtained as

$$\begin{cases} I^{+*}_{dMMC} = \dfrac{k^+_{id\_volMMC}(V^+_{dMMC}-V^{+*}_{dMMC})}{\sqrt{{k^+_{id\_volMMC}}^2(V^+_{dMMC}-V^{+*}_{dMMC})^2+{k^+_{iq\_volMMC}}^2(V^+_{qMMC}-V^{+*}_{qMMC})^2}} \times I^+_{\lim MMC} \\ I^{+*}_{qMMC} = \dfrac{k^+_{iq\_volMMC}(V^+_{qMMC}-V^{+*}_{qMMC})}{\sqrt{{k^+_{id\_volMMC}}^2(V^+_{dMMC}-V^{+*}_{dMMC})^2+{k^+_{iq\_volMMC}}^2(V^+_{qMMC}-V^{+*}_{qMMC})^2}} \times I^+_{\lim MMC} \end{cases} \tag{26}$$

$$\begin{cases} E^+_{dMMC} = \dfrac{-k^+_{id\_cur}(I^{+*}_{dMMC}-I^+_{dMMC})}{\sqrt{{k^+_{id\_cur}}^2(I^{+*}_{dMMC}-I^+_{dMMC})^2+{k^+_{iq\_cur}}^2(I^{+*}_{qMMC}-I^+_{qMMC})^2}} E^+_{\lim MMC} \\ E^+_{qMMC} = \dfrac{-k^+_{iq\_cur}(I^{+*}_{qMMC}-I^+_{qMMC})}{\sqrt{{k^+_{id\_cur}}^2(I^{+*}_{dMMC}-I^+_{dMMC})^2+{k^+_{iq\_cur}}^2(I^{+*}_{qMMC}-I^+_{qMMC})^2}} E^+_{\lim MMC} \end{cases} \tag{27}$$

where $k^+_{p\_curMMC}$ and $k^+_{i_curMMC}$are the PI coefficients of the current inner loop of the VF control.

D. Mathematical Expressions of Power Angle

In the transformation matrix, the power angle δ^+ should be expressed by the state and independent variables. For ease of calculation, two vector triangles are constructed at the fault point and the relationship between δ^+_{MMC} and δ^+_{WT} is established via the fault voltage vector $\boldsymbol{V}^+_F$, as shown in Fig. 6. By applying the law of sine, δ^+_{MMC} and δ^+_{WT} can be calculated by

$$\sin\delta^+_{MMC} = \frac{|\boldsymbol{I}^+_{MMC}|\,|\boldsymbol{Z}^+_{LMMC}+jX^+_{T1}|}{|\boldsymbol{V}^+_F|} \times \sin\left(\theta_{\boldsymbol{I}^+_{MMC}}+\theta_{(\boldsymbol{Z}^+_{LMMC}+jX^+_{T1})}-\theta_{\boldsymbol{V}^+_{MMC}}\right) \tag{28}$$

$$\sin\delta^+_{WT} = \frac{|\boldsymbol{I}^+_{WT}|\,|\boldsymbol{Z}^+_{WT}|}{|\boldsymbol{V}^+_F|}\sin\left(\varphi^+_{WT}+\theta_{\boldsymbol{Z}^+_{WT}}-\theta_{\boldsymbol{V}^+_{WT}}\right) \tag{29}$$

where

$$|\boldsymbol{V}^+_F| = \sqrt{{V^+_{dF}}^2+{V^+_{qF}}^2} \tag{30}$$

$$\begin{aligned} \begin{bmatrix} V^+_{dF} \\ V^+_{qF} \end{bmatrix} &= \begin{bmatrix} V^+_{dMMC} \\ V^+_{qMMC} \end{bmatrix} + R^+_{LMMC}\begin{bmatrix} I^+_{dMMC} \\ I^+_{qMMC} \end{bmatrix} \\ &\quad + \left(X^+_{LMMC}+X^+_{T1}\right)\begin{bmatrix} -I^+_{qMMC} \\ I^+_{dMMC} \end{bmatrix} \\ \text{or} &= \boldsymbol{T}_{WT-MMC}\left(\begin{bmatrix} V^+_{dWT} \\ V^+_{qWT} \end{bmatrix} - R^+_{WT}\begin{bmatrix} I^+_{dWT} \\ I^+_{qWT} \end{bmatrix} - X^+_{WT}\begin{bmatrix} -I^+_{qWT} \\ I^+_{dWT} \end{bmatrix}\right). \end{aligned} \tag{31}$$

Furthermore, δ^+ can be obtained as

$$\delta^+ = \delta^+_{MMC}+\delta^+_{WT}. \tag{32}$$

E. Static Stability Constraint of the PLL

In each mode, two steady-state operating points satisfying the algebraic equations are expected without considering the dynamic of the PLL [23], [41]. Therefore, the static stability of the PLL in different modes is essential and serves as a constraint to screen the valid steady-state operating point.

For the given PLL described in (5) and (6), $V^+_{dWT} > 0$ and $V^+_{qWT} = 0$ are satisfied in the steady state. Taking the CLM with the positive sequence current amplitude of the MMC limited to I^+_{limMMC} as an example, V^+_{qWT} can be obtained by KVL as

$$\begin{aligned} V^+_{qWT} &= \underbrace{I^+_{dWT}\left(X^{(m)}_F+X^+_{WT}\right)+I^+_{qWT}\left(R^{(m)}_F+R^+_{WT}\right)}_{\text{defined as } H^{CLM}_i} \\ &\quad -\underbrace{\left(\widehat{I}^+_{dMMC}X^{(m)}_F+\widehat{I}^+_{qMMC}R^{(m)}_F\right)}_{\text{defined as } H^{CLM}_o} \end{aligned} \tag{33}$$

where H^{CLM}_i and H^{CLM}_o are the input and output voltage of the PLL, respectively. Mapping the current of the MMC from the MMC frame to the WT frame holds

$$\begin{bmatrix} \widehat{I}^+_{dMMC} \\ \widehat{I}^+_{qMMC} \end{bmatrix}_{\theta^+_{WT}} = \boldsymbol{T}_{WT-MMC}{}^{-1}\begin{bmatrix} I^+_{dMMC} \\ I^+_{qMMC} \end{bmatrix}_{\theta^+_{MMC}}. \tag{34}$$

Substituting (34) into (33) yields

$$H^{CLM}_o = -I^+_{limMMC}\left|\boldsymbol{Z}^{(m)}_F\right|\cdot\sin\left(\delta^+ + \theta_{\boldsymbol{V}^+_{MMC}} - \theta_{\boldsymbol{Z}^{(m)}_F} - \theta_{\boldsymbol{I}^+_{MMC}}\right). \tag{35}$$

As illustrated in Fig. 7, the intersection points of the curves H^{CLM}_i and H^{CLM}_o determine the steady-state operating point, where the PLL can automatically stabilize at $V^+_{dWT} > 0$. This equilibrium, however, can be broken in the CLM due to the conflict between the current limiting function of the VF control and the dynamics of the PLL. Taking C4 in Table V as an example, Fig. 8 provides the vector diagram without considering the dynamics of the PLL. With the current limiting function, V^+_{WT} cannot return to the positive d-axis of the WT frame.

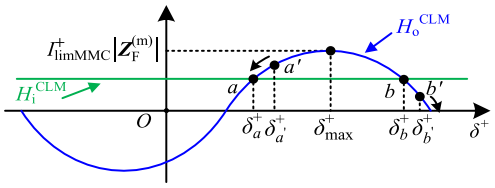

Fig. 7. Voltage–power angle curves of the CLM.

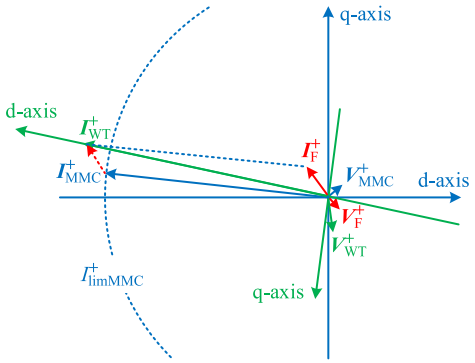

Fig. 8. Vector diagram when the equilibrium relationship of the PLL is broken in some regions. [Parameters: C4 in Table V].

Alternatively, once V^+_{WT} is forced to that position, the control equations of the CLM cannot be satisfied, meaning that the positive sequence current amplitude of the MMC cannot be limited to I^+_{limMMC}. This conflict can lead to the loss of steady-state operating points and induce divergent oscillations. Consequently, the following criterion must be satisfied to guarantee the existence of steady-state operating points:

$$\left|H_{\text{i}}^{\text{CLM}}\right| \le I^+_{\text{limMMC}}\left|\boldsymbol{Z}^{(\text{m})}_{\text{F}}\right| \,\&\, \boldsymbol{V}^+_{\text{WT}} \text{ is on the positive } d\text{-axis} \tag{36}$$

where & represents the logical AND.

It is observed from Fig. 7 that two intersection points exist, i.e., points a and b when $|H_{\text{i}}^{\text{CLM}}| < I^+_{\text{limMMC}}|\boldsymbol{Z}^{(\text{m})}_{\text{F}}|$. During a small disturbance, the operating point shifts from point a to point a', where $V^+_{\text{qWT}} < 0$, driving $\Delta\omega^+_{\text{WT}}$ to decrease and the operating point returns to a. Conversely, for point b', $V^+_{\text{qWT}} > 0$ and $\Delta\omega^+_{\text{WT}}$ increases, pushing the operating point to move further away from point b. Consequently, point a is statically stable while point b is not. Based on the analysis above, the static stability criterion of the CLM is that the slope of the curve $H_{\text{o}}^{\text{CLM}}$ is greater than 0, i.e.,

$$\frac{dH_{\text{o}}^{\text{CLM}}}{d\delta^+} = -I^+_{\text{limMMC}}\left|\boldsymbol{Z}^{(\text{m})}_{\text{F}}\right|\cos\left(\delta^+ + \theta_{\boldsymbol{V}^+_{\text{MMC}}} - \theta_{\boldsymbol{Z}^{(\text{m})}_{\text{F}}} - \theta_{\boldsymbol{I}^+_{\text{MMC}}}\right) \ge 0. \tag{37}$$

When $|H_{\text{i}}^{\text{CLM}}| > I^+_{\text{limMMC}}|\boldsymbol{Z}^{(\text{m})}_{\text{F}}|$, the PLL loses its steady-state operating point, where the frequency of the PLL will deviate from its rated value. Taking C5 in Table V as an example, $H_{\text{i}}^{\text{CLM}} = 0.2076$ and $I^+_{\text{limMMC}}|Z^{(\text{m})}_{\text{F}}| = 0.2012$, the criterion in (36) is not satisfied and oscillation occurs in the PLL of the WT, as shown in Fig. 9. In the MMC side, this oscillation

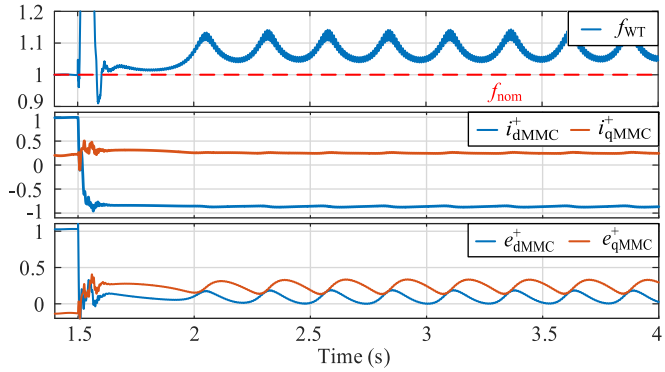

Fig. 9. Simulation waveforms when the PLL of the WT loses its steady-state operating point in the CLM. [Parameters: C5 in Table V. Units: p.u.].

causes the fluctuations, rather than divergent oscillations, of the dq-axes positive sequence terminal voltage and current near their steady-state operating points.

For the VCM and MVLM, the positive sequence PoC-MMC voltage and terminal voltage are controlled as V^{+*}_{dMMC} and E^+_{limMMC}, respectively, which remain constant. Therefore, the KVL equations originate from the PoC-MMC for the VCM and the terminal point for the MVLM. V^+_{qWT} can be derived as

$$V^+_{\text{qWT}} = \underbrace{I^+_{\text{dWT}}X^+_{\text{WT}} + I^+_{\text{qWT}}R^+_{\text{LWT}}}_{\text{defined as } H_{\text{i}}^{\text{VCM}}} - \underbrace{\left[-\widehat{V}^+_{\text{qMMC}} - \widehat{I}^+_{\text{dMMC}}\left(X^+_{\text{LMMC}} + X^+_{\text{T1}}\right) - \widehat{I}^+_{\text{qMMC}}R^+_{\text{LMMC}}\right]}_{\text{defined as } H_{\text{o}}^{\text{VCM}}} \tag{38}$$

$$V^+_{\text{qWT}} = \underbrace{I^+_{\text{dWT}}X^+_{\text{WT}} + I^+_{\text{qWT}}R^+_{\text{WT}}}_{\text{defined as } H_{\text{i}}^{\text{MVLM}}} - \underbrace{\left[-\widehat{E}^+_{\text{qMMC}} - \widehat{I}^+_{\text{dMMC}}X^+_{\text{MMC}} - \widehat{I}^+_{\text{qMMC}}R^+_{\text{MMC}}\right]}_{\text{defined as } H_{\text{o}}^{\text{MVLM}}}. \tag{39}$$

The expressions of H_{i}, A_{Ho}, and $dH_{\text{o}}/d\delta^+$ in the CLM, VCM, and MVLM are given in Table II. Unlike the CLM, a slack positive sequence current of the MMC in the VCM and MVLM inherently ensures that $\boldsymbol{V}^+_{\text{WT}}$ is locked to the positive d-axis of the WT frame.

IV. Analysis of the Weak Grid Characteristic

In this section, the weak grid characteristic is analyzed by numerical traversal. The parameters of the studied system are listed in Table III.

A. Solving Method of the State Variables

In the studied system, the state variables are decomposed into dq-axes components $\boldsymbol{X} = [I^+_{\text{dMMC}}, I^+_{\text{qMMC}},$

TABLE II
VARIABLES FOR EXISTENCE RANGE AND STATIC STABILITY CRITERION OF STEADY-STATE OPERATING POINTS OF PLL

Operating modes	H_i	A_{Ho}	$dH_o/d\delta^+$
	Existence range of steady-state operating points: $\lvert H_i\rvert \le A_{Ho}$ & $\boldsymbol{V}^+_{WT}$ is in the positive d-axis Static stability criterion: $dH_o/d\delta^+ \ge 0$		
CLM	$I^+_{dWT}\,(X^{(m)}_F + X^+_{WT})$ $+\,I^+_{qWT}\,(R^{(m)}_F + R^+_{WT})$	$I^+_{limMMC}\,\lvert \boldsymbol{Z}^{(m)}_F\rvert$	$-I^+_{limMMC}\,\lvert \boldsymbol{Z}^{(m)}_F\rvert\cos(\delta^+ + \theta_{\boldsymbol{V}^+_{MMC}} - \theta_{\boldsymbol{Z}^{(m)}_F} - \theta_{\boldsymbol{I}^+_{MMC}})$
VCM	$I^+_{dWT}\,X^+_{WT} + I^+_{qWT}\,R^+_{WT}$	$\sqrt{V^{+*}_{dMMC}{}^2 + \lvert \boldsymbol{I}^+_{MMC}\rvert^2\lvert \boldsymbol{Z}^+_{LMMC} + jX^+_{T1}\rvert^2 + 2V^{+*}_{dMMC}\lvert \boldsymbol{I}^+_{MMC}\rvert\lvert \boldsymbol{Z}^+_{LMMC} + jX^+_{T1}\rvert\cos\left(\theta_{(\boldsymbol{Z}^+_{LMMC}+jX^+_{T1})} + \theta_{\boldsymbol{I}^+_{MMC}}\right)}$	$V^{+*}_{dMMC}\cos\delta^+ + \lvert \boldsymbol{I}^+_{MMC}\rvert\lvert \boldsymbol{Z}^+_{LMMC} + jX^+_{T1}\rvert\cos(\delta^+ - \theta_{(\boldsymbol{Z}^+_{LMMC}+jX^+_{T1})} - \theta_{\boldsymbol{I}^+_{MMC}})$
MVLM	$I^+_{dWT}\,X^+_{WT} + I^+_{qWT}\,R^+_{WT}$	$\sqrt{E^{+}_{limMMC}{}^2 + \lvert \boldsymbol{I}^+_{MMC}\rvert^2\lvert \boldsymbol{Z}^+_{MMC}\rvert^2 + 2E^+_{limMMC}\lvert \boldsymbol{I}^+_{MMC}\rvert\lvert \boldsymbol{Z}^+_{MMC}\rvert\cos(\theta_{\boldsymbol{Z}^+_{MMC}} + \theta_{\boldsymbol{I}^+_{MMC}} - \theta_{\boldsymbol{E}^+_{MMC}})}$	$E^+_{limMMC}\cos(\delta^+ + \theta_{\boldsymbol{V}^+_{MMC}} - \theta_{\boldsymbol{E}^+_{MMC}}) + \lvert \boldsymbol{I}^+_{MMC}\rvert\lvert \boldsymbol{Z}^+_{MMC}\rvert\cos(\delta^+ + \theta_{\boldsymbol{V}^+_{MMC}} - \theta_{\boldsymbol{Z}^+_{MMC}} - \theta_{\boldsymbol{I}^+_{MMC}})$

TABLE III
MAIN PARAMETERS OF THE STUDIED SYSTEM

Parameters		Values	p.u.
		Base capacity S_b=1000 MVA	
MMC	Base voltage V_b = 187.76 kV	Base current I_b = 3.55 kA	
	Nominal voltage (l-l, rms)	230 kV	$\sqrt{3}/\sqrt{2}$
	Dc voltage	±250 kV	1
	Arm inductance	45 mH	0.2672
	Maximum allowable current I_{maxMMC}	/	1.1
	Maximum available modulation voltage for MVL E_{maxMMC}	/	1.3
	PI coefficients of the positive sequence voltage loop controller $k^+_{p\_volMMC}/k^+_{i\_volMMC}$	/	1.2/100
	PI coefficients of the positive sequence current loop controller $k^+_{p\_curMMC}/k^+_{i\_curMMC}$	/	0.8/5
	PI coefficients of the ACC $k^-_{p\_ACCMMC}/k^-_{i\_ACCMMC}$	/	0.25/2
WT	Base voltage V_b = 563.28 V	Base current I_b = 1183.11 kA	
	Nominal voltage (l-l, rms)	690 V	$\sqrt{3}/\sqrt{2}$
	PI coefficients of the positive sequence current inner loop controller $k^+_{p\_curWT}/k^+_{i\_curWT}$	/	0.6/15
	PI coefficients of the ACC $k^-_{p\_ACCWT}/k^-_{i\_ACCWT}$	/	0.6/10
	PI coefficients of the PLL $k^+_{p\_PLL}/k^+_{i\_PLL}$	/	300/50
AC line	Base voltage V_b = 187.76 kV	Base current I_b = 3.55 kA	
	Transmission line parameters (per km)	0.02 Ω/ 0.076 mH	0.000378/ 0.000451
	Transmission line length	20 km	/
	Positive, negative, and zero sequence reactance of the transformers X_{T1}/X_{T2}	5.8055 Ω/ 4.4965 Ω	0.109745/ 0.085
	Transformer ratios k_{T1}/k_{T2}	230 kV/230 kV 230 kV/690 V	/

$V^+_{dMMC}, V^+_{qMMC}, E^+_{dMMC}, E^+_{qMMC}]^T$ and the others are independent variables and system parameters. Network equations, connection equations, and control equations have been set up to numerically calculate the state variables and determine the operating modes using the vpasolve function in MATLAB. During the solving process of the state variables, two prerequisites exist as follows.

1) The obtained solutions must adhere to the static stability requirements, as provided in Table II.
2) In the vicinity of $Z^{(m)}_F = 0$, i.e., $U(0, \varepsilon) = \{\boldsymbol{Z}^{(m)}_F \mid \lvert \boldsymbol{Z}^{(m)}_F - 0\rvert < \varepsilon\}$, where ε is a positive infinitesimal, the WT and MMC are loosely correlated or even completely decoupled. Under this circumstance, the network equations are split to (40) and (41), separately describing the networks on the MMC and WT sides. Even when the steady-state operating point of the PLL in the WT is lost, the VF control of the MMC will not be affected, and the solutions to the state variables will exist. In other words, oscillations only occur in the WT.

$$\begin{bmatrix} E^+_{dMMC} \\ E^+_{qMMC} \end{bmatrix} = -\begin{bmatrix} R^+_{MMC} & -X^+_{MMC} \\ X^+_{MMC} & R^+_{MMC} \end{bmatrix}\begin{bmatrix} I^+_{dMMC} \\ I^+_{qMMC} \end{bmatrix} \tag{40}$$

$$\begin{bmatrix} V^+_{dWT} \\ V^+_{qWT} \end{bmatrix} = \begin{bmatrix} R^+_{WT} & -X^+_{WT} \\ X^+_{WT} & R^+_{WT} \end{bmatrix}\begin{bmatrix} I^+_{dWT} \\ I^+_{qWT} \end{bmatrix} \tag{41}$$

To identify the operating modes and steady-state operating points of the MMC and WT, the proposed method first assumes an initial mode, solves the state variables, and then determines the validity of the assumption based on the solutions. With the CL-VSR limiting structure, according to the response process of the VF control, it is reasonable to select the VCM as its initial mode. If the result indicates that the positive sequence current amplitude reaches or exceeds its limit, it can be concluded that the MMC is in the CLM. The flowchart is provided in Fig. 10.

Similarly, with the CL-MVL limiting structure, the solving mode is set as the VCM, CLM, and MVLM sequentially, as shown in Fig. 11. The first determination is made based on whether both the positive sequence current and terminal voltage stay within their limits. If so, the MMC operates in the VCM. Otherwise, change the solving mode to the CLM and repeat the process. Then, check if a solution exists and if the solved positive sequence terminal voltage is below its limit. If so, the MMC is in the CLM. Otherwise, further try the solving mode of the MVLM and check if a solution exists or $\lvert H^{CLM}_i\rvert > I^+_{limMMC}\lvert \boldsymbol{Z}^{(m)}_F\rvert$. If so, the MMC operates in the MVLM, otherwise it remains in the CLM.

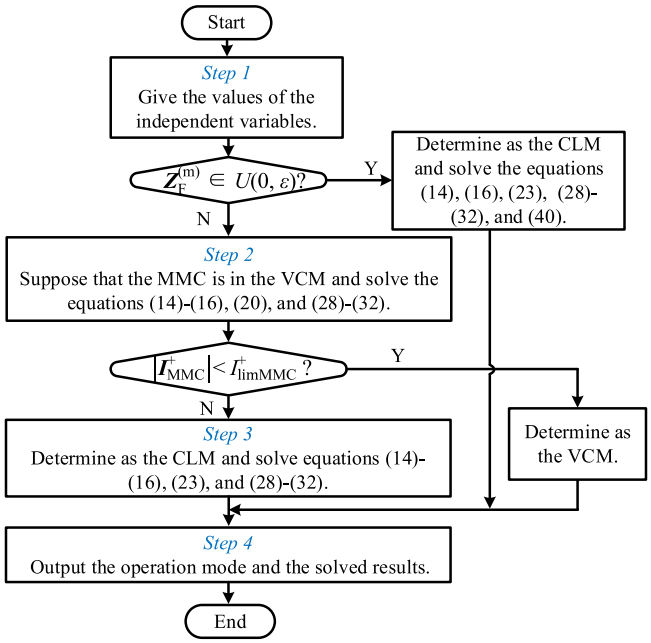

Fig. 10. Flowchart of judging operating mode and solving state variables with the CL-VSR limiting structure.

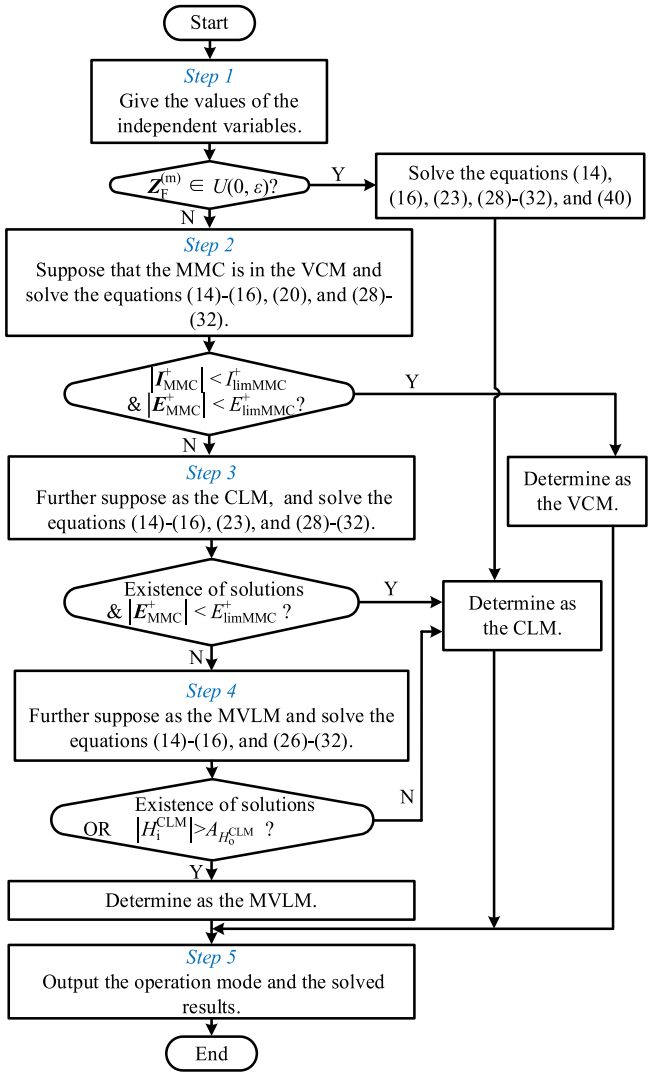

Fig. 11. Flowchart of judging operating mode and solving state variables with the CL-MVL limiting structure.

B. Weak Grid Characteristic With the CL-VSR Limiting Structure

Figs. 12–14 show the graphical solutions of the positive sequence terminal voltage and current amplitudes of the MMC with the CL-VSR limiting structure. The voltage and current values for the CLM cases with no valid solution are set to zero, representing oscillating conditions. Unlike a power grid, the positive sequence terminal voltage of the MMC is no longer constant; instead, it experiences amplitude drops and oscillations due to physical constraints, which manifests the weak grid characteristic as previously discussed. To elaborate on the weak grid characteristic, the VCM, CLM, and MVLM are further subdivided into four regions: the stiff region, low GFI region, overcurrent region, and the loss of the steady-state operating point of the PLL (LOSSOP-PLL) in the CLM, respectively, highlighted in light blue, green, grey, and dark blue in the subfigures. On this basis, the weak grid characteristic is explained in detail as follows.

Stiff and Low GFI Regions: The VCM exhibits a relatively constant amplitude of the positive sequence terminal voltage, stabilizing at around V_{dMMC}^{+*} (0.5 p.u. in this study), without any oscillations. Thus, this region is defined as the stiff region and $|I_{MMC}^+| = I_{limMMC}^+$ is satisfied along its boundary. As illustrated in Figs. 12 and 13, when $|I_{WT}^+| > I_{limMMC}^+$, the stiff region is within the boundary; otherwise, it is outside the boundary. After hitting the CL, the VF control goes across the VCM boundary and into the CLM. In this mode, the amplitude of the positive sequence current is constant at I_{limMMC}^+ (0.9 p.u. in this study), while the positive sequence terminal voltage collapses as the GFI drops to nearly zero. The amplitude drop in the weak grid characteristic is primarily attributed to the low GFI region.

LOSSOP-PLL in the CLM: When there is no steady-state operating point of the PLL in the CLM, i.e., beyond the curves of $|H_i^{CLM}| = A_{H_o^{CLM}}$, no solution exists, leading to oscillations on the WT side and nondivergent fluctuations in the MMC. Particularly, at $Z_F^{(m)} = 0$, the positive sequence terminal voltage amplitude of the MMC is calculated to be 0.2190 p.u., and an oscillation still occurs on the WT side, as shown in Fig. 12(c).

Overcurrent Region: Another type of oscillation occurs in the overcurrent region of the CLM. When the MMC receives a positive sequence current with amplitude exceeding I_{limMMC}^+, the VF control dynamically adjusts and elevates its terminal voltage to enhance the current sharing of the fault branch. Unlike the low GFI region solely relying on the CL, the current limiting function in the overcurrent region strongly depends on the fault branch and can only be achieved under certain GFIs, as shown in Fig. 12(d). In such cases, however, the overvoltage occurs simultaneously. Under other GFIs, the steady-state terminal voltage cannot be established, resulting in no solution to the

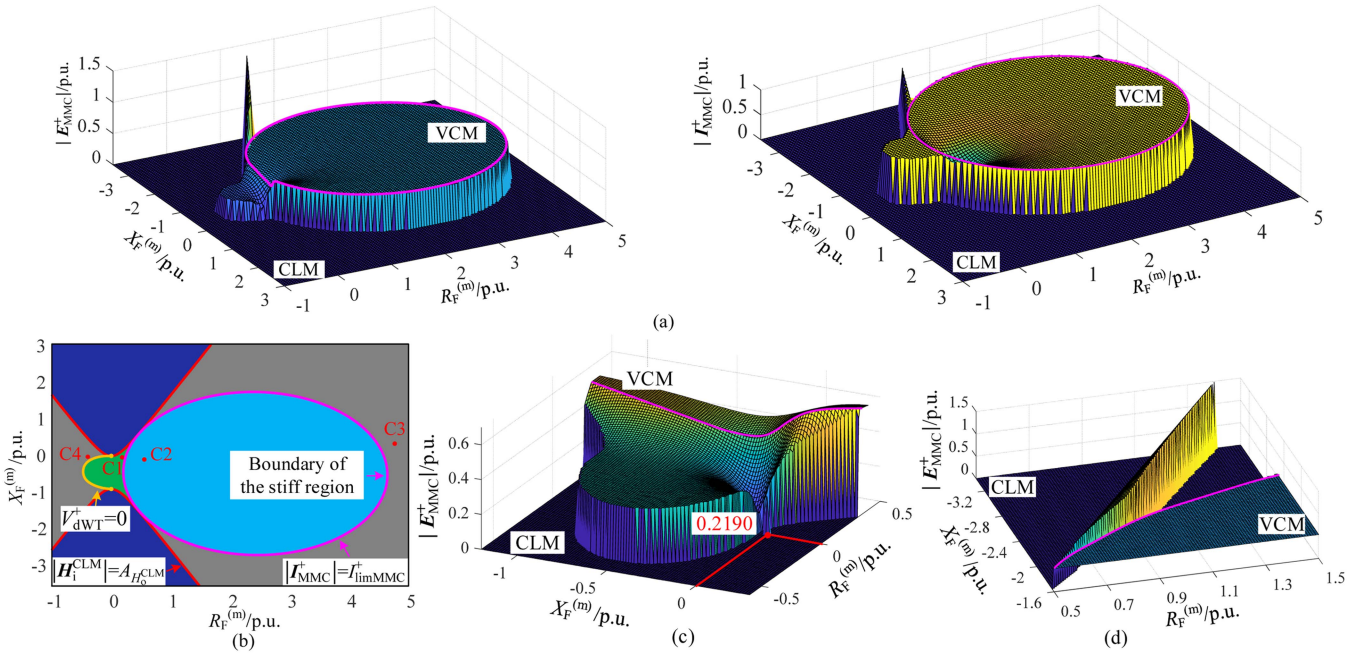

Fig. 12. Graphical solution with the CL-VSR limiting structure under a specific positive sequence current of the WT with its amplitude exceeding I^{+}_{limMMC}. [Parameters: $\alpha = 0\%$, $I^{+}_{limMMC} = 0.9$ p.u., $V^{+*}_{dMMC} = 0.5$ p.u., $|\boldsymbol{I}^{+}_{WT}| = 1$ p.u., $\varphi^{+}_{WT} = 0$ deg]. (a) Overall view of the positive sequence terminal voltage and current amplitudes. (b) Region divisions with the boundaries. (c) Zoomed-in view of the low GFI region. (d) Zoomed-in view of solutions existing in the overcurrent region.

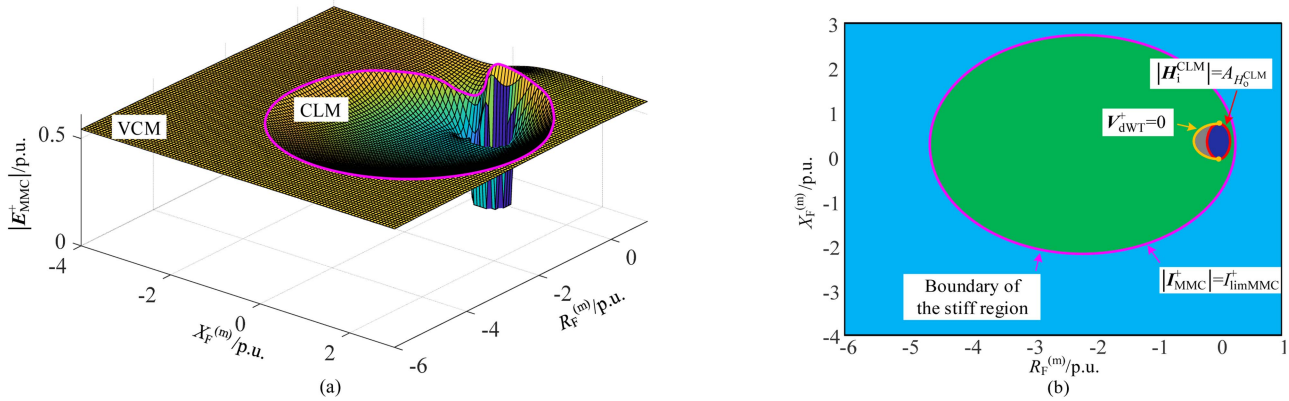

Fig. 13. Graphical solution with the CL-VSR limiting structure under a specific positive sequence current of the WT with its amplitude less than I^{+}_{limMMC}. [Parameters: $\alpha = 0\%$, $I^{+}_{limMMC} = 0.9$ p.u., $V^{+*}_{dMMC} = 0.5$ p.u., $|\boldsymbol{I}^{+}_{WT}| = 0.8$ p.u., $\varphi^{+}_{WT} = 0$ deg]. (a) Overall view of the positive sequence terminal voltage amplitude. (b) Region divisions with the boundaries.

equations of the CLM and divergent oscillations in the MMC. It is worth mentioning that the conflict between the current limiting function of the VF control and the dynamics of the PLL, as discussed in Section III-E, also occurs in the overcurrent region.

As shown in Fig. 14(a), the amplitude of the positive sequence terminal voltage varies with the phase angle of the WT positive sequence current, and a greater positive sequence current induces a larger variation in the amplitude of the positive sequence terminal voltage. Once the current amplitude exceeds I^{+}_{limMMC}, the WT is at a significant risk of entering the LOSSOP-PLL and overcurrent regions, as shown in Fig. 14(b).

C. Weak Grid Characteristic With the CL-MVL Limiting Structure

This subsection primarily focuses on the distinct weak grid characteristic introduced by the MVL when $V^{+*}_{dMMC} = 1$. Figs. 15 and 16 show the graphical solutions with the CL-MVL limiting structure, and the value of the MVL varies.

When the MVL is set as 1.1 p.u., there is a sufficient dc voltage margin for the positive sequence terminal voltage in the stiff region, as shown in Fig. 15(a). However, when the negative sequence modulation voltage margin increases and the MVL drops to 0.8 p.u., the positive sequence terminal voltage

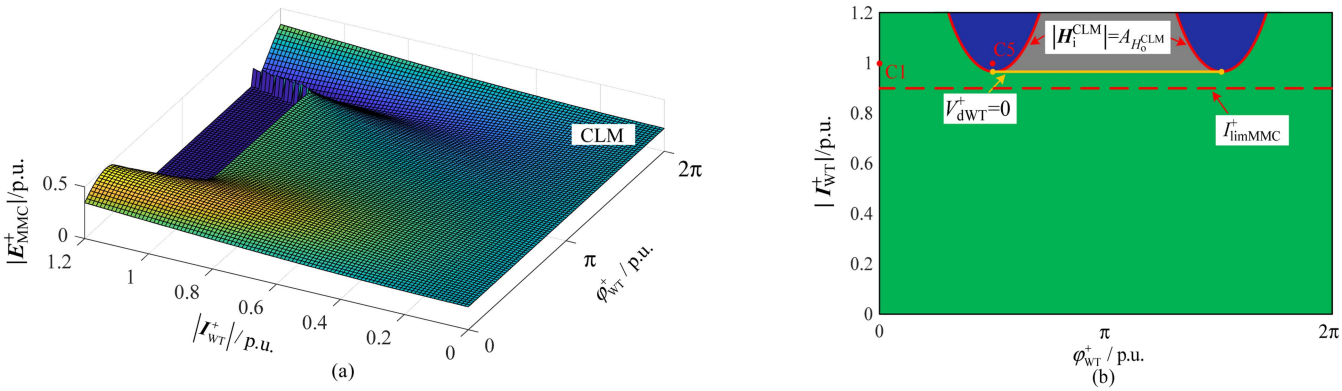

Fig. 14. Graphical solution with the CL-VSR limiting structure under a specific GFI. [Parameters: $\alpha = 0\%$, $I^{+}_{\text{limMMC}} = 0.9$ p.u., $V^{+*}_{\text{dMMC}} = 0.5$ p.u., $R^{(\text{m})}_{\text{F}} = 0.2$ p.u., $X^{(\text{m})}_{\text{F}} = -0.1$ p.u.]. (a) Overall view of the positive sequence terminal voltage amplitude. (b) Region divisions with the boundaries.

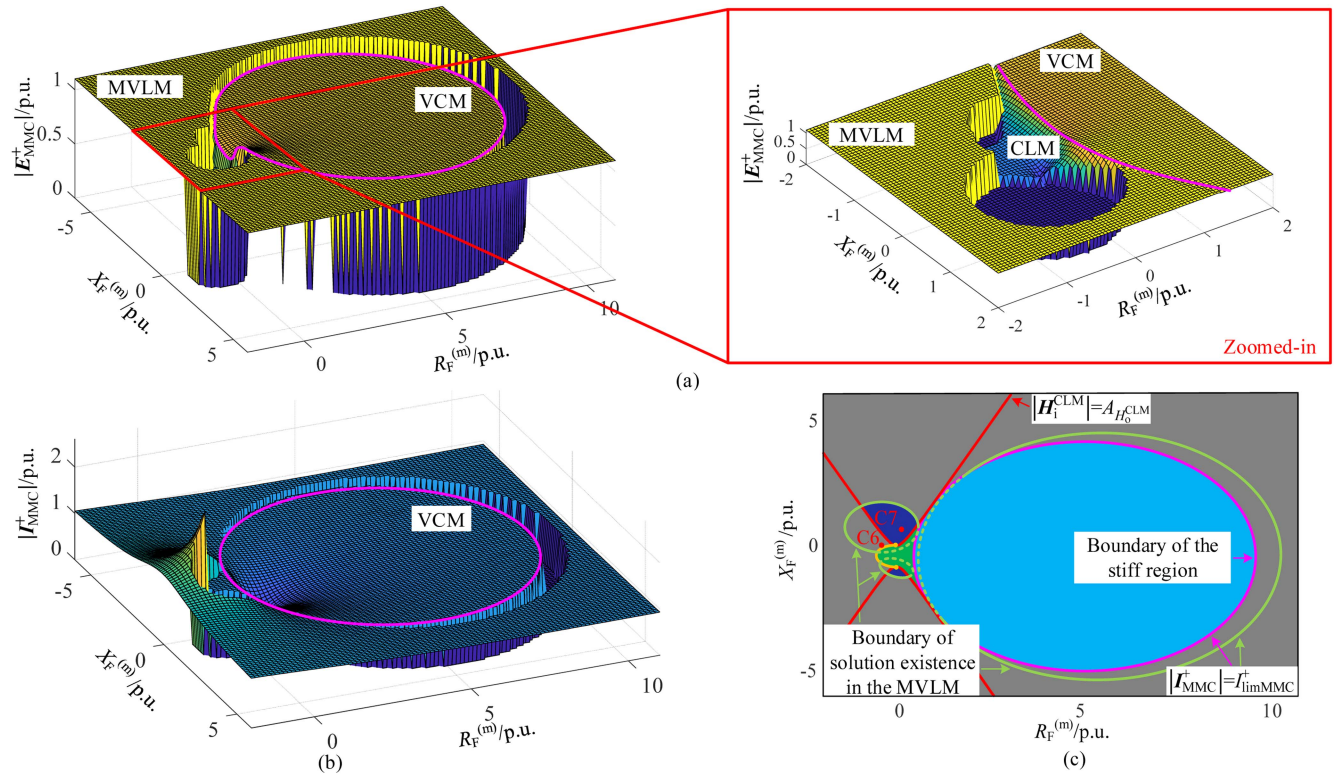

Fig. 15. Graphical solutions with the CL-MVL limiting structure under a specific positive sequence current of the WT under $E^{+}_{\text{limMMC}} = 1.1$ p.u. [Parameters: $\alpha = 0\%$, $I^{+}_{\text{limMMC}} = 0.9$ p.u., $|\boldsymbol{I}^{+}_{\text{WT}}| = 1$ p.u., $\varphi^{+}_{\text{WT}} = 0$ deg]. (a) Overall view of the positive sequence terminal voltage amplitude. (b) Overall view of the current amplitude. (c) Region divisions with the boundaries.

amplitude hits its limit, causing the MMC to transition from the VCM to the MVLM, as shown in Fig. 16(a). Consequently, whether the VF control operates in the VCM or MVLM is entirely determined by the MVL settings.

Both the divergent oscillations and nondivergent fluctuations in the MMC can be mitigated by adjusting the MVL, which forms the steady-state operating point and gives a positive sequence terminal voltage of the MMC with a constant amplitude ($= E^{+}_{\text{limMMC}}$). The premise is that the positive sequence terminal voltage must reach its limit, and solutions of the MVLM must exist. Otherwise, oscillations persist, such as 1) around the low GFI region and 2) around the boundary of the stiff region. As shown in the zone surrounded by green lines in Fig. 15(c), there are three no-solution zones in the MVLM, with two zones around the low GFI region and one zone around the boundary of the stiff region. As the MVL decreases, the latter zone shrinks or even disappears, as shown in Fig. 16(c). Such process indicates that the MVL cannot reach saturation before the CL, as discussed in Section III-C. Additionally, due to the loss of the positive sequence current control capability in the MVLM, the oscillating

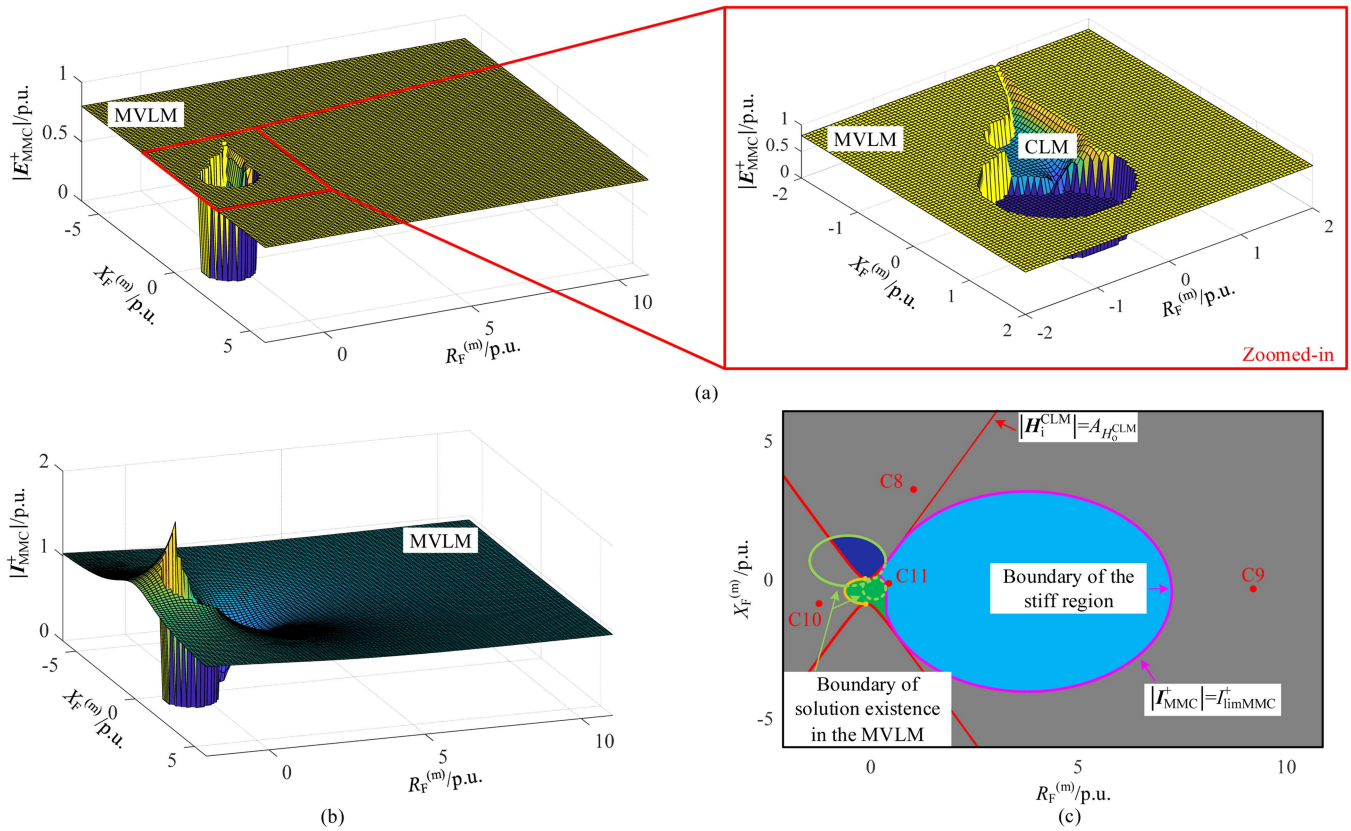

Fig. 16. Graphical solutions with the CL-MVL limiting structure under a specific positive sequence current of the WT under $E^{+}_{\text{limMMC}} = 0.8$ p.u. [Parameters: $\alpha = 0\%$, $I^{+}_{\text{limMMC}} = 0.9$ p.u., $|\boldsymbol{I}^{+}_{\text{WT}}| = 1$ p.u., $\varphi^{+}_{\text{WT}} = 0$ deg]. (a) Overall view of the positive sequence terminal voltage amplitude. (b) Overall view of the current amplitude. (c) Region divisions with the boundaries.

conditions transition to overcurrent conditions. Consequently, the feasible regions have not been expanded despite the introduction of the MVL.

D. Conclusions on the Weak Grid Characteristic

The weak grid characteristic is reflected in the following three aspects:

1) *Feasible Regions:* As physically constrained by the dc voltage and current capacity of the MMC, two feasible regions are formed: the stiff region, referring to the VCM or nonovercurrent portion of the MVLM, and the low GFI region, corresponding to the solution-existence portion of the CLM. The former region requires a higher GFI, while the latter necessitates a lower GFI. The boundary of the stiff region is determined by the type and limit value of the CL, which also serves as the mode boundary between the VCM and the CLM/MVLM, as well as the overcurrent boundary in the MVLM. The low GFI region is surrounded by the curves of $V^{+}_{\text{dWT}} = 0$, $|H^{\text{CLM}}_{\text{i}}| = A_{H^{\text{CLM}}_{\text{o}}}$, and the boundary of the stiff region.
2) *Infeasible Regions:* There are two types of oscillations in the *infeasible regions*: 1) the MMC faces a positive sequence current injection with amplitude exceeding I^{+}_{limMMC}; and 2) the PLL of the WT loses the steady-state operating point, i.e., $|H^{\text{CLM}}_{\text{i}}| > A^{\text{CLM}}_{H_{\text{o}}}$. The former induces divergent oscillations in the positive sequence terminal voltage, while the latter causes nondivergent fluctuations. They both can be suppressed by the MVL when the positive sequence terminal voltage hits the MVL and the steady-state operating point of the MMC exists, i.e., oscillation conditions transition to overcurrent conditions, which, however, remain unavailable.
3) *Conflicts Among Positive Sequence Current and Voltage Limit Values and Negative Sequence Equivalent Impedance in the MMC:* As compared in Figs. 12(b), 15(c), and 16(c), a higher positive sequence voltage can expand the stiff region by increasing the current sharing of the fault branch and mitigating current stresses, but it requires a higher dc voltage. In contrast, the negative sequence circuit is composed of impedances and thus exhibits simultaneous increases or decreases in the negative sequence voltage and current under a given negative sequence impedance. Additionally, a higher positive sequence voltage also leads to an increased negative sequence current and modulation voltage, which in turn restrict the positive sequence current and voltage limit values. The reduction of the *d*-axis voltage setpoint or the settings of the MVL can also result in the amplitude drop of the positive sequence voltage in the weak grid

TABLE IV
COMPARISONS BETWEEN THE STIFF REGION AND THE LOW GFI REGION

Feasible regions	Stiff region	Low GFI region
Operating mode	VCM or MVLM	CLM
Application scenarios	Priority selection under high GFI conditions (Note: VCM pertains to low negative sequence modulation voltage, while MVLM is the opposite)	Maximum fault voltage support under low GFI conditions
Voltage stiffness	High	Low
Current stiffness	Low	High
Voltage control capability	High	Low
Positive sequence current capacity utilization	Partial	Full
Availability under symmetric condition	Yes	No

characteristic. The conflicts must be considered when designing positive sequence limit values and negative sequence equivalent impedance.

Due to the identical feasible and infeasible regions, as well as the same reductions in the positive sequence current and voltage for the negative sequence margins in the MMC, the two limiting structures exhibit consistency in the weak grid characteristic.

V. MODE SELECTION FOR VOLTAGE SUPPORT CONSIDERING THE WEAK GRID CHARACTERISTIC

According to the analysis in Section IV, the positive sequence terminal voltage, respectively, adheres to distinct evolution principles in the two feasible regions. Moreover, due to the presence of numerous nonlinear terms, deriving a precise analytical expression for the positive sequence terminal voltage concerning the independent variables is quite challenging. As a result, repeatedly navigating across the boundary between the two feasible regions to globally identify the optimal operating point in real time for the maximum voltage support imposes a significant computational burden on the controllers. To streamline this process, it is essential to determine the target feasible region, i.e., the operating mode, prior to the voltage support realization.

Table IV compares the stiff region and the low GFI region. The stiff region is prioritized for its high voltage stiffness, high voltage control capability, and ability to operate continuously during the transition between symmetric and asymmetric conditions. However, since the stiff region requires a higher GFI, once certain faults forcibly lower the GFI, rendering this region inaccessible, the low GFI region becomes a backup option. In this context, high current stiffness and full utilization of the positive sequence current capacity ensure maximum voltage support under the low GFI condition. Both the negative sequence equivalent impedance and the fault/grounding impedance can contribute to the GFI, and their interaction depends on the type of asymmetric faults. Therefore, the fault type and fault/grounding impedance are two crucial indicators for mode selection. Considering the structure and parameters in the GFI branch, the following mode selection method is proposed for different types of asymmetric faults.

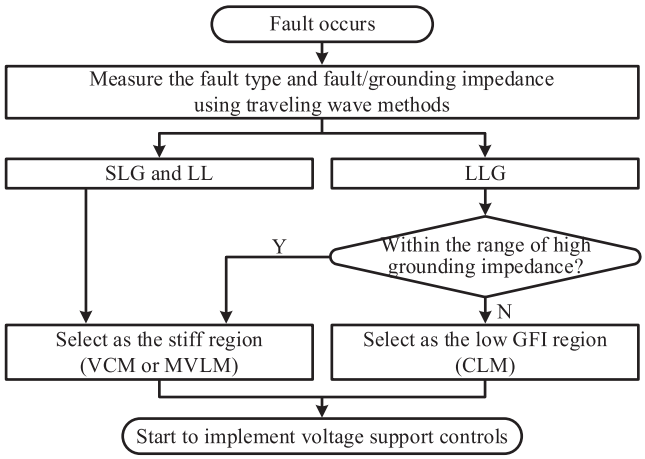

Fig. 17. Operating mode selection procedure under different types of faults.

1) Under the SLG and LL, the GFI can be higher than the fault/grounding impedance as the negative sequence circuit is connected in series. Consequently, the SLG and LL can exhibit high GFIs via the negative sequence control and enable operation in the stiff region. However, raising the negative sequence equivalent impedance to increase the GFI can lead to a higher negative sequence modulation voltage, narrowing the boundary of the stiff region. From this perspective, the SLG is less severe than the LL due to a larger voltage sharing of the fault/grounding impedance.
2) Under the LLG, the GFI is lower than the grounding impedance because the negative sequence circuit operates in parallel, resulting in a low GFI that forces operation in the low GFI region. However, when the grounding impedance is sufficiently high, the GFI can still operate in the stiff region by implementing high negative sequence equivalent impedances in both the MMC and WT. Drawing on the high grounding impedance defined under symmetric faults in [25], a conservative range of the high grounding impedance under the LLG is established as follows. The amplitude of the positive sequence PoC-MMC voltage is assumed to be over 0.9 p.u. when a fault occurs at the MMC terminal, supported by a full positive sequence current from the MMC (zero from the WT) and infinity negative sequence equivalent impedance, i.e.,

$$\left|\boldsymbol{V}_{\mathrm{MMC}}^{+}\right| = \left|jX_{\mathrm{T1}}^{+} + jX_{\mathrm{T1}}^{0} // \left(jX_{\mathrm{T2}}^{0} + \boldsymbol{Z}_{\mathrm{L}}^{0}\right) + 3\boldsymbol{Z}_{\mathrm{g}}\right| I_{\mathrm{limMMC}} \geq 0.9. \tag{42}$$

Fig. 17 illustrates the mode selection procedure. It is worth noting that the fault types and fault/grounding impedance are measurable using traveling wave methods [42], [43], with a measuring time within 100 μs (the length of the ac collection line is on the order of ten kilometers [22]). With this mode selection method, the process of seeking the optimal voltage support point occurs solely within the target feasible region.

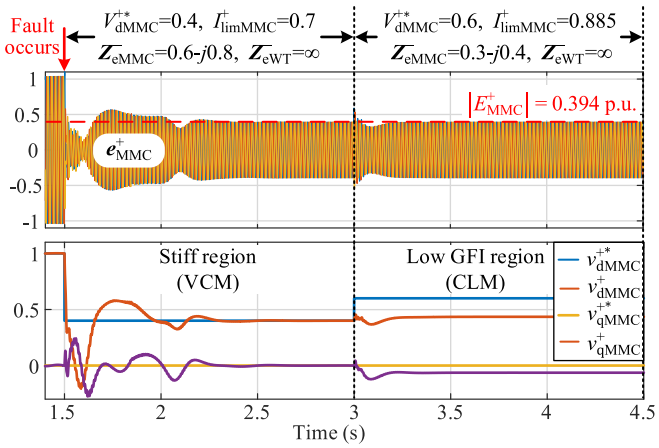

Fig. 18. Simulation waveforms with the grounding impedance marginally below the conservative range. [Parameters: $R_g = 0.2$ p.u., $|\boldsymbol{I}^{+}_{WT}| = 1$ p.u., $\varphi^{+}_{WT} = 0$ deg. Units: p.u.].

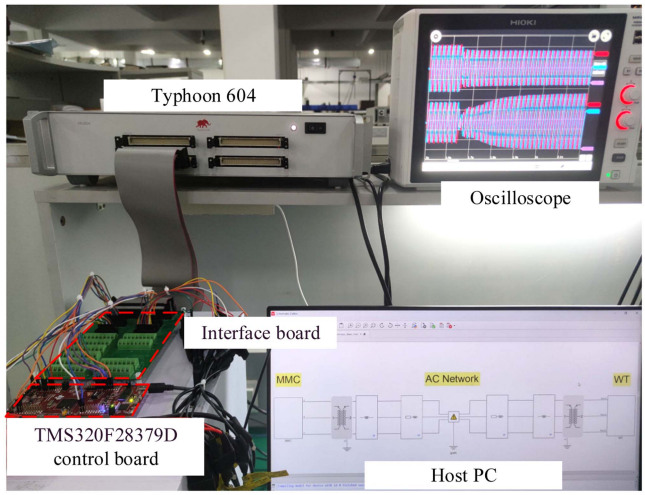

Fig. 19. CHIL setup used in the experiments.

With the grounding impedance marginally below the conservative range in (42), the reserved negative sequence margins can adjust the settings of the CL and MVL or d-axis set-point, as presented in (17), (18) and (24), to achieve the same amplitude of the positive sequence terminal voltage in either mode. Taking the system parameters given in Table III as an example and assuming a resistive grounding impedance, the range of the high grounding impedance is calculated as $R_g \geq 0.2667$ p.u. As shown in Fig. 18, when R_g is set as 0.2 p.u., both the stiff and low GFI regions can be accessed, and the amplitudes of the positive sequence terminal voltage in both regions are equal to 0.394 p.u. Therefore, the expansion of the selected range within the low GFI region, caused by the conservatism of the critical impedance, cannot affect the optimal voltage support point. Additionally, the ambiguous boundary between the stiff region and the low GFI region can enhance the measurement error tolerance of the traveling wave measurement device.

VI. CHIL Experimental Verification

In this section, the validity of the proposed modeling method and the weak grid characteristic is verified through CHIL experiments, with the main parameters listed in Table III. To simplify the experimental model, the dc cables, receiving-end MMC, and the main power grid are substituted by a constant dc voltage source. The positive and negative sequence controls of the MMC are implemented on a TMS320F28379D control board, while the other elements are simulated in Typhoon 604, including the power stages of the MMC and WT, the ac network, and the positive and negative sequence controls of the WT. The sampling rate of the DSP is configured at 5 k, and that of the Typhoon 604 is set at 20 k. The positive and negative sequence components of the voltages and currents are extracted with a dual second-order generalized integrator [44]. The test setup of the CHIL is presented in Fig. 19. Eleven typical fault cases are studied in Table V under different fault types, fault/grounding impedances, limiting structures, MVL settings, equivalent impedances of the negative sequence controls, and positive sequence currents of the WT, corresponding to operating points in Figs. 12–16. It is worth mentioning that the infinite negative sequence equivalent impedance in the MMC is realized by setting zero negative sequence equivalent admittance reference in the ACC.

CHIL experimental waveforms with the CL-VSR and CL-MVL limiting structures are shown in Figs. 20 and 21, respectively. The experimental and numerical calculation results are summarized in Table VI, which shows strong consistency. In all cases with solutions (C1-C2 and C8–C11), the absolute error is less than 0.008 p.u. (i.e., minimum increment of the oscilloscope cursor), demonstrating the accuracy of the modeling method.

When the CL-VSR limiting structure is utilized, as the operating point transitions from the stiff region [C1, Fig. 20(a)] to the low GFI region [C2, Fig. 20(b)], and then to the LOSSOP-PLL region [C5, Fig. 20(e)], the positive sequence terminal voltage of the MMC reduces and finally oscillates due to the lack of valid solution. The three stages illustrated in Fig. 2, respectively, correspond to these three regions. For C3 and C4 in the overcurrent region, the divergent oscillations occur in the positive sequence terminal voltage of the MMC. Although the diverging three-phase terminal voltage can be limited by the dc voltage, as shown in Fig. 20(c) and (d), the MMC has already been out of control. Unlike C3, the divergent oscillation of the positive sequence terminal voltage develops in C4 mainly because of the conflict between the current limiting function of the VF control and the dynamics of the PLL. These phenomena validate the weak grid characteristic with the CL-VSR limiting structure.

For the CL-MVL limiting structure, despite the introduction of the MVL, a steady-state operating point is still not available in the overcurrent region [C6, Fig. 21(a)] and LOSSOP-PLL region [C7, Fig. 21(b)] around the zero GFI, and oscillations remain. For C8–C10 in the overcurrent region, within the boundary of solution existence in the MVLM, steady-state operating points are formed by the MVL, with the amplitude of the positive sequence terminal voltage limited to E^{+}_{limMMC} (= 0.8 p.u., in this

TABLE V
CASE SETTINGS OF THE CL-VSR AND THE CL-MVL LIMITING STRUCTURES

No.	Limiting structures	Limit values/ voltage references (p.u.)	Fault conditions (Locations $\alpha = 0\%$)		Equivalent impedances of negative sequence controls		GFIs $\underline{Z}_{\mathrm{F}}^{(\mathrm{m})}$/p.u.	Positive sequence currents of the WT ($\boldsymbol{I}_{\mathrm{WT}}^{+}$)		Regions in Figs. 12–16
		$I_{\mathrm{limMMC}}^{+} = 0.9$ p.u.	Types	$\underline{Z}_{\mathrm{g}}$/ p.u.	MMC $\underline{Z}_{\mathrm{eMMC}}$/ p.u.	WT $\underline{Z}_{\mathrm{eWT}}$/ p.u.		Amplitudes $\lvert\boldsymbol{I}_{\mathrm{WT}}^{+}\rvert$/ p.u.	angles $\varphi_{\mathrm{WT}}^{+}$/ deg	
C1	CL-VSR	$V_{\mathrm{dMMC}}^{+*} = 0.5$	LLG	0.0001	∞	−0.001223 − *j*0.139289	0.2000 − *j*0.1000	1.0	0	CLM (Low GFI region)
C2		$V_{\mathrm{dMMC}}^{+*} = 0.5$	LL	0.0001	∞	0.5190 − *j*0.2768	0.5267 − *j*0.1828	1.0	0	VCM (Stiff region)
C3		$V_{\mathrm{dMMC}}^{+*} = 0.5$	SLG	0.1000	8.0000 + *j*0.5000	10.0000 + *j*0.5000	4.7484 + *j*0.3563	1.0	0	CLM (Overcurrent region)
C4		$V_{\mathrm{dMMC}}^{+*} = 0.5$	SLG	0.0001	∞	−0.5000 − *j*0.2000	−0.4899 − *j*0.0553	1.0	0	CLM (Overcurrent region)
C5		$V_{\mathrm{dMMC}}^{+*} = 0.5$	LLG	0.0001	∞	−0.001223 − *j*0.139289	0.2000 − *j*0.1000	1.0	$\pi/2$	CLM (LOSSOP-PLL region)
C6	CL-MVL	$E_{\mathrm{limMMC}}^{+} = 1.1$	SLG	0.1000	∞	−0.7997 − *j*0.2000	−0.4899 − *j*0.0553	1.0	0	MVLM (Overcurrent region)
C7		$E_{\mathrm{limMMC}}^{+} = 1.1$	LL	0.3000	∞	−0.2276 + *j*0.5160	0.0800 + *j*0.6100	1.0	0	CLM (LOSSOP-PLL region)
C8		$E_{\mathrm{limMMC}}^{+} = 0.8$	LL	0.3000	0.2000 + *j*6.0000	3.0000 + *j*6.0000	1.0639 + *j*3.2024	1.0	0	MVLM (Overcurrent region)
C9		$E_{\mathrm{limMMC}}^{+} = 0.8$	LL	5.0000	∞	4.2124 − *j*0.4740	9.2200 − *j*0.3800	1.0	0	MVLM (Overcurrent region)
C10		$E_{\mathrm{limMMC}}^{+} = 0.8$	LL	0.3000	∞	−1.5000 − *j*1.0000	−1.1924 − *j*0.9060	1.0	0	MVLM (Overcurrent region)
C11		$E_{\mathrm{limMMC}}^{+} = 0.8$	LL	0.1000	∞	0.4191 − *j*0.2768	0.5267 − *j*0.1828	1.0	0	MVLM (Stiff region)

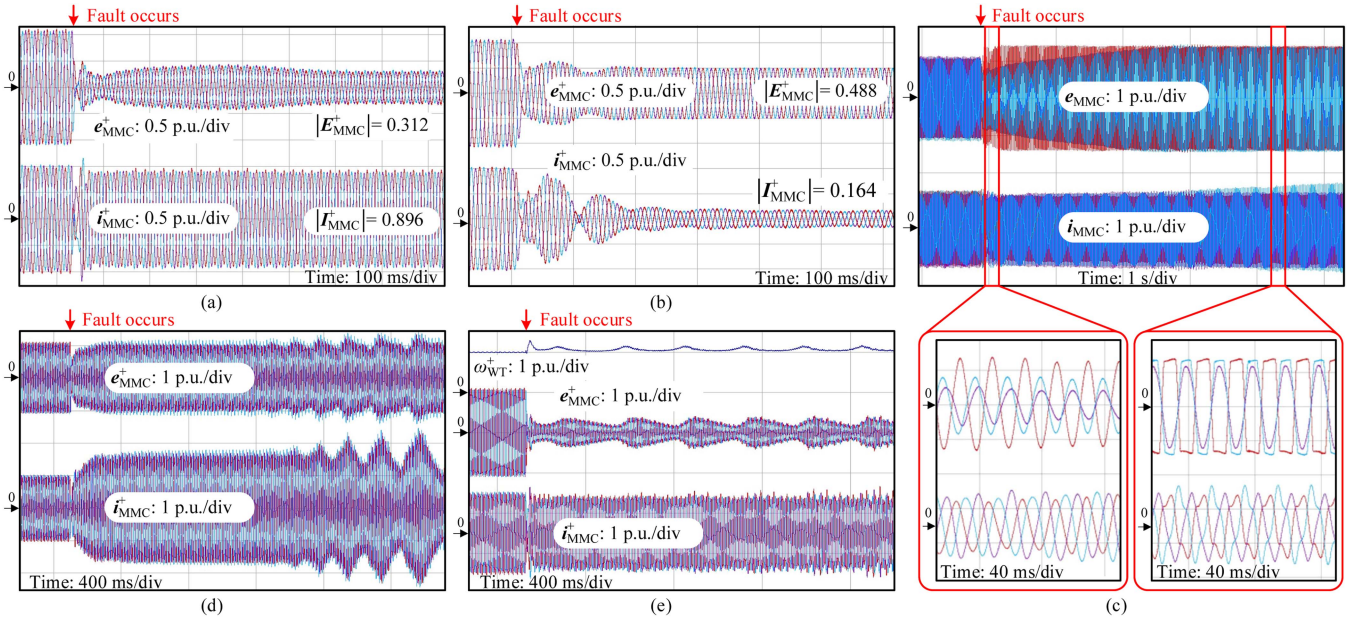

Fig. 20. CHIL experimental results with the CL-VSR limiting structure. (a)–(b) and (d)–(e) Positive sequence components of there-phase voltage and current. (c) There-phase voltage and current.

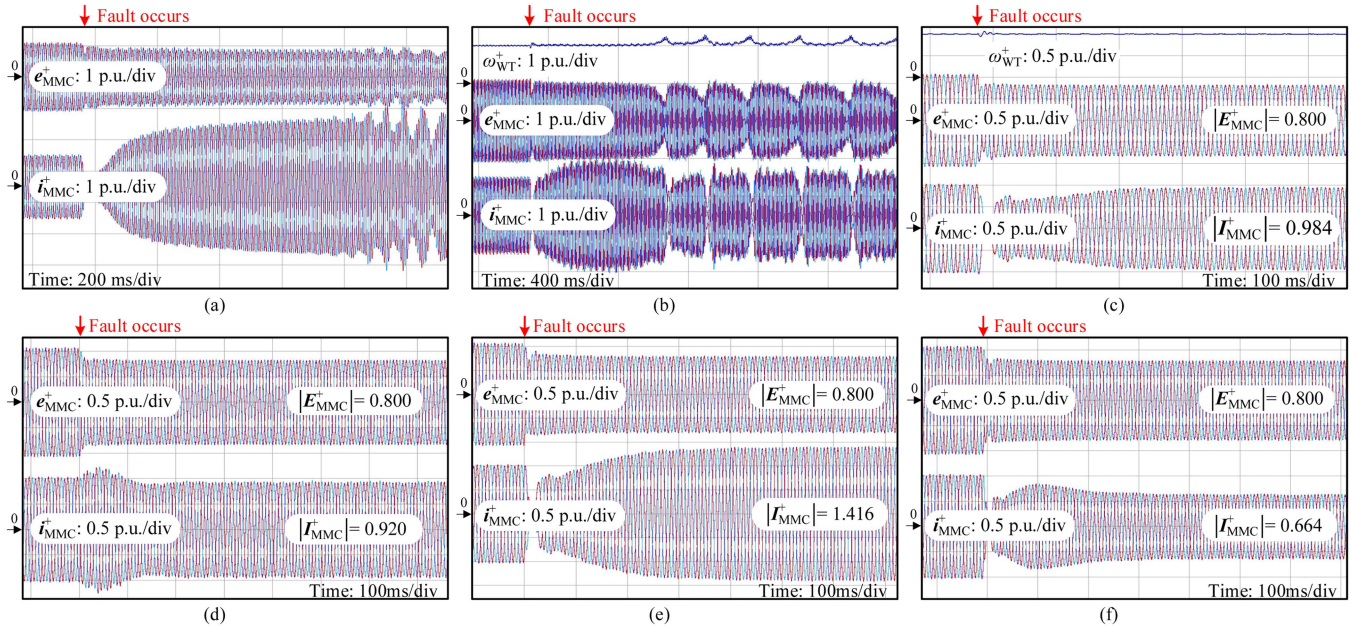

Fig. 21. CHIL experimental results with the CL-MVL limiting structure. (a)–(f) Positive sequence components of there-phase voltage and current.

TABLE VI
CHIL EXPERIMENTAL AND NUMERICAL CALCULATION RESULTS

No.	CHIL experiment results	Numerical calculation results			Operating modes
	$\|E^+_{MMC}\|$, $\|I^+_{MMC}\|$/p.u.	V^+_{dMMC}, V^+_{qMMC}, I^+_{dMMC} (I^{+*}_{dMMC}), I^+_{qMMC} (I^{+*}_{qMMC}), E^+_{dMMC}, E^+_{qMMC} /p.u.	$\|V^+_{MMC}\|$, $\|I^+_{MMC}\|$, $\|E^+_{MMC}\|$/p.u.	Power angle δ^+/ rad	
C1	0.312, 0.896	0.3501, –0.0557, –0.8437 (–0.8437), –0.3132 (–0.3132), 0.3082, 0.0571	0.3545, 0.9000, 0.3134	0.0198	CLM
C2	0.488, 0.164	0.5000, 0.0000, 0.1170 (0.1170), –0.1153 (–0.1153), 0.4846, –0.0156	0.5000, 0.1643, 0.4849	0.2094	VCM
C3	Oscillating condition	No solution	/	No solution	CLM (Oscillation)
C4	Oscillating condition	No solution	/	No solution	CLM (Oscillation)
C5	Oscillating condition	No solution	/	No solution	CLM (Oscillation)
C6	Oscillating condition	No solution	/	No solution	MVLM (Oscillation)
C7	Oscillating condition	No solution	/	No solution	CLM (Oscillation)
C8	0.800, 0.984	0.7049, 0.1921, 0.7209 (–0.7543), 0.6689 (0.4910), 0.7942, 0.0958	0.7306, 0.9834, 0.8000	0.2769	MVLM (Overcurrent)
C9	0.800, 0.920	0.7502, 0.1132, 0.8414 (–0.8198) 0.3729 (0.3713), 0.8000, 0.0008	0.7587, 0.9203, 0.8000	0.2600	MVLM (Overcurrent)
C10	0.800, 1.416	0.7499, 0.1487, 1.3651 (–0.7736) 0.3698 (0.4599), 0.7993, –0.0337	0.7645, 1.4143, 0.8000	0.3251	MVLM (Overcurrent)
C11	0.800, 0.664	0.8455, –0.0642, –0.5715 (–0.8311), –0.3414 (–0.3453), 0.7999, 0.0122	0.8479, 0.6657, 0.8000	0.0386	MVLM

study), which leads to overcurrent, as shown in Fig. 21(c)–(e). Additionally, since there is no sufficient dc voltage margin, the amplitude of the positive sequence terminal voltage in the stiff region [C11, Fig. 21(f)] is also limited to 0.8 p.u. These phenomena validate the weak grid characteristic with the CL-MVL limiting structure.

VII. CONCLUSION

In the sending-end MMC-WTs system, the weak grid characteristic diminishes the grid-forming capability of the MMC, rendering the voltage support control methods designed for grid-connected inverters ineffective. To elaborate on the weak

grid characteristic during voltage support, this article establishes a GFI-based mathematical modeling method, defines the potential operating modes, and proposes a numerical traversal method to solve the state variables. The study of the weak grid characteristic reveals that only the stiff region in the VCM or MVCM and the low GFI region in the CLM are feasible. The former mode is desirable under the SLG, LL, and LLG with a high grounding impedance, while the latter is preferable under the LLG with a low grounding impedance.

The proposed modeling and analysis methods are also applicable to symmetric faults. In this context, the GFI degrades into a passive and uncontrollable grounding impedance. For a resistive-inductive grounding impedance, the GFI stays in the first quadrant; for a purely resistive grounding impedance, the GFI is on the positive $R_{\mathrm{F}}^{(\mathrm{m})}$-axis. Therefore, symmetric faults can be treated as a particular case of asymmetric faults. Additionally, the mode selection method for symmetric faults is similar to that of the LLG.

Future work involves the control optimization of the MMC and WT to promote the voltage support performance, utilizing the steady-state mathematical model, feasible regions, and operating mode selection method proposed in this article. In addition, this article only deals with the steady-state operation points, but the sending-end MMC-WTs system must undergo a transient process prior to this. Therefore, ensuring transient stability under different controls will be another important area.

REFERENCES

[1] S. Debnath, J. Qin, B. Bahrani, M. Saeedifard, and P. Barbosa, "Operation control and applications of the modular multilevel converter: A review," *IEEE Trans. Power Electron.*, vol. 30, no. 1, pp. 37–53, Jan. 2015.

[2] Z. He, J. Hu, L. Lin, P. Zeng, and L. Hang, "A generalized DC asymmetrical fault analysis method for MMC-HVDC grids considering metallic return conductors," *IEEE Trans. Power Del.*, vol. 39, no. 5, pp. 2568–2579, Oct. 2024.

[3] H. Zhao et al., "Multi-stage sequential network energy control for offshore AC asymmetric fault ride-through of MMC-HVDC system integrated offshore wind farms," *Int. J. Elect. Power Energy Syst.*, vol. 151, Mar. 2023, Art. no. 109180.

[4] *IEEE Standard for Interconnection and Interoperability of Distributed Energy Resources with Associated Electric Power Systems Interfaces*, IEEE Std 1547-2018, 2018.

[5] VDE (Association for Electrical, Electronic and Information Technologies), "VDE-AR-N 4110: Technical rules for the connection of customer systems to the medium voltage network and its operation (TAR medium voltage)," Nat. Legislation, Berlin, Germany, Sep. 2023.

[6] *Technical Specification for Connecting Wind Farm to Power System – Part 1: On Shore Wind Power*, GB/T 19963.1-2021, Standard Admin. China, Beijing, China, Aug. 2021.

[7] Y. Liu, J. Hu, W. He, Y. Zhou, and M. Zhan, "Local load effect on the DC voltage control timescale oscillation of voltage source converters," *IEEE Trans. Power Syst.*, to be published, doi: 10.1109/TPWRS.2025.3597612.

[8] Y. Zhang and M. Zhan, "Transient synchronous stability analysis of PMSG grid-connected system considering transient switching control under severe faults," *IEEE Trans. Power Electron.*, vol. 40, no. 5, pp. 7298–7314, May 2025.

[9] Z. Zeng, J. Fan, Y. Sun, S. Wang, and D. Yang, "A dispatchable virtual oscillator controller in the dq frame with enhanced grid-forming power reference tracking capability," *IEEE Trans. Power Electron.*, vol. 40, no. 8, pp. 10973–10987, Aug. 2025.

[10] Z. Lin, R. Liu, and Y. R. Li, "Transient stability analysis and coordinated phase control method for multi-parallel PLL-synchronized inverters during grid fault," *IEEE Trans. Power Electron.*, vol. 40, no. 8, pp. 11442–11451, Aug. 2025.

[11] *Wind Turbines- Test Procedure of Voltage Fault Ride Through Capability*, GB/T 36995-2018, Standard Admin. China, Dec. 2018.

[12] A. Camacho, M. Castilla, J. Miret, R. Guzman, and A. Borrell, "Reactive power control for distributed generation power plants to comply with voltage limits during grid faults," *IEEE Trans. Power Electron.*, vol. 29, no. 11, pp. 6224–6234, Nov. 2014.

[13] M. M. Shabestary and Y. A.-R. I. Mohamed, "An analytical method to obtain maximum allowable grid support by using grid-connected converters," *IEEE Trans. Sustain. Energy*, vol. 7, no. 4, pp. 1558–1571, Oct. 2016.

[14] M. M. Shabestary and Y. A.-R. I. Mohamed, "Analytical expressions for multiobjective optimization of converter-based DG operation under unbalanced grid conditions," *IEEE Trans. Power Electron.*, vol. 32, no. 9, pp. 7284–7296, Sep. 2017.

[15] M. Islam, M. Nadarajah, and M. J. Hossain, "A grid-support strategy with PV units to boost short-term voltage stability under asymmetrical faults," *IEEE Trans. Power Syst.*, vol. 35, no. 2, pp. 1120–1131, Mar. 2020.

[16] A. Camacho, M. Castilla, J. Miret, L. G. de Vicuña, and R. Guzman, "Positive and negative sequence control strategies to maximize the voltage support in resistive–inductive grids during grid faults," *IEEE Trans. Power Electron.*, vol. 33, no. 6, pp. 5362–5373, Jun. 2018.

[17] X. Guo, X. Zhang, B. Wang, W. Wu, and J. M. Guerrero, "Asymmetrical grid fault ride-through strategy of three-phase grid-connected inverter considering network impedance impact in low-voltage grid," *IEEE Trans. Power Electron.*, vol. 29, no. 3, pp. 1064–1068, Mar. 2014.

[18] M. M. Shabestary and Y. A.-R. I. Mohamed, "Autonomous coordinated control scheme for cooperative asymmetric low-voltage ride-through and grid support in active distribution networks with multiple DG units," *IEEE Trans. Smart Grid*, vol. 11, no. 3, pp. 2125–2139, May 2020.

[19] M. M. Shabestary and Y. A.-R. I. Mohamed, "Maximum asymmetrical support in parallel-operated grid-interactive smart inverters," *IEEE Trans. Sustain. Energy*, vol. 13, no. 1, pp. 14–30, Jan. 2022.

[20] J. N. Sakamuri, Z. H. Rather, J. Rimez, M. Altin, Ö. Göksu, and N. A. Cutululis, "Coordinated voltage control in offshore HVDC connected cluster of wind power plants," *IEEE Trans. Sustain. Energy*, vol. 7, no. 4, pp. 1592–1601, Oct. 2016.

[21] E. Sánchez-Sánchez, E. Prieto-Araujo, and O. Gomis-Bellmunt, "The role of the internal energy in MMCs operating in grid-forming mode," *IEEE J. Emerg. Sel. Topics Power Electron.*, vol. 8, no. 2, pp. 949–962, Jun. 2020.

[22] L. Shi, G. P. Adam, R. Li, and L. Xu, "Control of offshore MMC during asymmetric offshore AC faults for wind power transmission," *IEEE J. Emerg. Sel. Topics Power Electron.*, vol. 8, no. 2, pp. 1074–1083, Jun. 2020.

[23] F. Li, L. Lin, Y. Li, X. Shi, J. Hu, and J. Zhu, "Synchronization stability of the MMC-connected wind farm under severe asymmetrical faults," *IEEE J. Emerg. Sel. Topics Circuits Syst.*, vol. 13, no. 3, pp. 680–691, Sep. 2023.

[24] J. Yan et al., "Overcurrent suppression method for multiple wind farms connected to MMC-HVDC," *IEEE Trans. Circuits Syst. II, Exp. Briefs*, vol. 69, no. 11, pp. 4473–4477, Nov. 2022.

[25] Y. Li et al., "PLL synchronization stability analysis of MMC-connected wind farms under high-impedance AC faults," *IEEE Trans. Power Syst.*, vol. 36, no. 3, pp. 2251–2261, May 2021.

[26] Y. Li et al., "Over-voltage suppression methods for the MMC-VSC-HVDC wind farm integration system," *IEEE Trans. Circuits Syst. II, Exp. Briefs*, vol. 67, no. 2, pp. 355–359, Feb. 2020.

[27] J. Yan, X. Shi, T. Liu, Z. Wang, T. Yin, and L. Lin, "Negative sequence impedance emulation: A new perspective and control," *IEEE Trans. Power Electron.*, vol. 39, no. 10, pp. 12135–12142, Oct. 2024.

[28] A. Adib, B. Mirafzal, X. Wang, and F. Blaabjerg, "On stability of voltage source inverters in weak grids," *IEEE Access*, vol. 6, pp. 4427–4439, 2018.

[29] S. Zhou et al., "An improved design of current controller for LCL-type grid-connected converter to reduce negative effect of PLL in weak grid," *IEEE J. Emerg. Sel. Topics Power Electron.*, vol. 6, no. 2, pp. 648–663, Jun. 2018.

[30] X. Zhang, D. Xia, Z. Fu, G. Wang, and D. Xu, "An improved feedforward control method considering PLL dynamics to improve weak grid stability of grid-connected inverters," *IEEE Trans. Ind. Appl.*, vol. 54, no. 5, pp. 5143–5151, Sep./Oct. 2018.

[31] A. Adib, F. Fateh, and B. Mirafzal, "Smart inverter stability enhancement in weak grids using adaptive virtual-inductance," *IEEE Trans. Ind. Appl.*, vol. 57, no. 1, pp. 814–823, Jan./Feb. 2021.

[32] T. Hossen and B. Mirafzal, "Hidden modes of instability for inverters in weak grids," *IEEE Trans. Ind. Appl.*, vol. 59, no. 4, pp. 4505–4515, Jul./Aug. 2023.

[33] L. Huang, H. Xin, Z. Wang, L. Zhang, K. Wu, and J. Hu, "Transient stability analysis and control design of droop-controlled voltage source converters considering current limitation," *IEEE Trans. Smart Grid*, vol. 10, no. 1, pp. 578–591, Jan. 2019.
[34] E. Rokrok, T. Qoria, A. Bruyere, B. Francois, and X. Guillaud, "Transient stability assessment and enhancement of grid-forming converters embedding current reference saturation as current limiting strategy," *IEEE Trans. Power Syst.*, vol. 37, no. 2, pp. 1519–1531, Mar. 2022.
[35] G. Wang, L. Fu, Q. Hu, C. Liu, and Y. Ma, "Transient synchronization stability of grid-forming converter during grid fault considering transient switched operation mode," *IEEE Trans. Sustain. Energy*, vol. 14, no. 3, pp. 1504–1515, Jul. 2023.
[36] P. Sun, Z. Tian, M. Huang, X. Zha, X. Li, and W. Wang, "Additional kinetic energy injection and piecewise damping based postfault antiwindup and transient stability enhanced control for grid-forming inverter," *IEEE Trans. Power Electron.*, vol. 39, no. 7, pp. 8007–8023, Jul. 2024.
[37] Y. Liu, H. Geng, C. He, W. Ding, C. Shen, and G. Yang, "Equivalent aggregated modeling of multi-VSC system for transient synchronization stability analysis," *IEEE Trans. Power Syst.*, vol. 39, no. 2, pp. 4296–4310, Mar. 2024.
[38] W. Li, P. Chao, X. Liang, J. Ma, D. Xu, and X. Jin, "A practical equivalent method for DFIG wind farms," *IEEE Trans. Sustain. Energy*, vol. 9, no. 2, pp. 610–620, Apr. 2018.
[39] T. Wu, Q. Jiang, M. Huang, and X. Xie, "Synchronization stability of grid-following converters governed by saturation nonlinearities," *IEEE Trans. Power Syst.*, vol. 37, no. 5, pp. 4102–4105, Sep. 2022.
[40] H. Sun, X. Lin, and J. Wei, "Transient synchronization stability and enhanced-LVRT scheme for grid-forming converters considering current limitation and nonlinear damping simultaneously," *IEEE Trans. Energy Convers.*, vol. 40, no. 3, pp. 2466–2484, Sep. 2025.
[41] Y. Li, C. Lin, J. Hu, and J. Guo, "PLL synchronization stability of grid-connected VSCs under asymmetric AC faults," *IEEE Trans. Energy Convers.*, vol. 37, no. 4, pp. 2438–2448, Dec. 2022.
[42] O. D. Naidu and A. K. Pradhan, "Precise traveling wave-based transmission line fault location method using single-ended data," *IEEE Trans. Ind. Inform.*, vol. 17, no. 8, pp. 5197–5207, Aug. 2021.
[43] H. A. Abd el-Ghany, A. M. Azmy, and A. M. Abeid, "A general travelling-wave-based scheme for locating simultaneous faults in transmission lines," *IEEE Trans. Power Del.*, vol. 35, no. 1, pp. 130–139, Feb. 2020.
[44] P. Rodríguez, A. Luna, R. S. Muñoz-Aguilar, I. Etxeberria-Otadui, R. Teodorescu, and F. Blaabjerg, "A stationary reference frame grid synchronization system for three-phase grid-connected power converters under adverse grid conditions," *IEEE Trans. Power Electron.*, vol. 27, no. 1, pp. 99–112, Jan. 2012.

Jianan Yan (Student Member, IEEE) was born in Dalian, Liaoning, China, in 1997. He received the B.S. and M.S. degrees in electrical engineering, in 2020 and 2023, respectively, from the School of Electrical and Electronics Engineering (SEEE), Huazhong University of Science and Technology (HUST), Wuhan, China, where he is currently working toward the Ph.D. degree in electrical engineering.

His research interests include fault ride-through (FRT) for wind farms connected to MMC-HVDC.

Xiaojie Shi (Senior Member, IEEE) received the M.S. degree in electrical engineering from Zhejiang University, Hangzhou, China, in 2011, and the Ph.D. degree in electrical engineering from University of Tennessee, Knoxville, TN, USA, in 2015.

She is currently a Full Professor with the Huazhong University of Science and Technology (HUST), Wuhan, China. Prior to joining HUST, she was with the Center for Ultra-Wide-Area Resilient Electric Energy Transmission Networks (CURENT), University of Tennessee, as a Research Assistant Professor in 2016, and with the Electric Power Research Institute (EPRI), Knoxville, as an Engineer/Scientist II from 2017 to 2019, and an Engineer/Scientist III from 2020 to 2021. Since 2019, she has also been an Adjunct Professor with the University of Tennessee. She has authored or coauthored more than 60 publications in international conferences and journals. Her research interests include microgrids, HVDC, and grid integration of renewable energy resources.

Dr. Shi was the recipient of more than 10 awards from EPRI and IEEE.

Tao Liu (Student Member, IEEE) was born in Huainan, Anhui, China, in 1999. He received the B.S. degree in electrical engineering from North China Electric Power University (NCEPU), Beijing, China, in 2022. He is currently working toward the Ph.D. degree in electrical engineering with the Huazhong University of Science and Technology (HUST), Wuhan, China.

His research interests include transient stability analysis and control of grid-forming converter-based power systems.

Zhiqiang (Jack) Wang (Senior Member, IEEE) received the B.S. degree in electrical engineering from Hunan University, Changsha, China, in 2007, and the M.S. degree in electrical engineering from Zhejiang University, Hangzhou, China, in 2010, and the Ph.D. degree from the University of Tennessee, Knoxville, TN, USA, in 2015.

He is currently a Full Professor with the Huazhong University of Science and Technology (HUST), Wuhan, China. Prior to joining HUST, he was with the Power Electronics and Electric Machinery Research Center, Oak Ridge National Laboratory (ORNL), Oak Ridge, TN, USA, as a Postmaster Research Associate, from 2014 to 2015, a full-time R&D Associate Staff Member from 2015 to 2018, and an R&D Staff Member in 2019. Since 2018, he has also been an Adjunct Professor with the University of Tennessee. He has authored and coauthored more than 80 publications in international conferences and journals. His research interests include packaging and integration of wide bandgap power semiconductor devices, and its applications to high-temperature, high-frequency, and high-density power electronics systems.

Dr. Wang was the recipient of more than ten awards from ORNL and IEEE. He was the Technical Program Chair for WiPDA-Asia 2021 conference and is currently the Transaction Paper Review Chair for the IEEE IAS Power Electronics Devices and Components Committee.

Li Zhang (Senior Member, IEEE) received the B.S. and Ph.D. degrees in electrical engineering from the Nanjing University of Aeronautics and Astronautics, Nanjing, China, in 2011 and 2017, respectively.

From 2017 to 2019, he was with the University of Tennessee, Knoxville, TN, USA. In 2019, he joined Nanyang Technological University, Singapore, and became a Research Assistant Professor, in 2022. Since July 2022, he has been a Full Professor with the Huazhong University of Science and Technology (HUST), Wuhan, China. His research interests include dc−dc conversion, SiC/GaN power conversion, and renewable energy generation systems.

Lei Lin (Senior Member, IEEE) was born in Jiangxi, China, in 1980. He received the B.S., M.S., and Ph.D. degrees in electrical engineering from the School of Electrical and Electronics Engineering (SEEE), Huazhong University of Science and Technology (HUST), Wuhan, China, in 2001, 2004, and 2007, respectively.

Since 2007, he has been involved in the teaching and research in the field of power electronics with SEEE, HUST, where he was a Postdoctoral Fellow from 2007 to 2009 and a Lecturer from 2009 to 2010. In 2010 and 2017, he was promoted to an Associate Professor and a Professor, respectively, with the State Key Laboratory of Advanced Electromagnetic Engineering and Technology, SEEE, HUST. He has authored or coauthored more than 60 technical articles, and holds over 20 issued/pending patents. His current research interests include a modular multilevel converter (MMC) for high-voltage direct-current (HVDC) applications, high-voltage capacitor charging power supply, multilevel converters, and related control techniques.

Dr. Lin is the Director of the Youth Working Committee of the China Power Supply Society. He is also an Active Expert of the IEEE UPFC P2745 Series.